2019
Volume 2
Issue 2
ISSN: 2578-2010

APPLIED CHEMICAL ENGINEERING

Volume 2 Issue 2 https://systems.enpress-publisher.com/index.php/ACE

ISSN 2578-2010
02
9 772578 201028

ACE

EnPress Publisher

Editorial Board

Editor-in-Chief

Associate Editor

Editorial Board Member

Volume 2 Issue 2 • 2019

Applied Chemical Engineering

EnPress Publisher

2019 | Volume 2 | Issue 2

Applied Chemical Engineering

https://systems.enpress-publisher.com/index.php/ace/

Contents

Original Research Article

Applied Chemical Engineering (2019) Volume 2 Issue 2
doi: 10.63019/ace.v1i2.584

Advancement of khadi textile: Textile glummer of India

M. Das[1], S. Basak[2]

[1] Assistant Director, National Accreditation Board for Testing and Calibration Laboratories, Haryana: 122002, India
[2] Scientist, Central Institute for Research on Cotton Technology, Adenwala Road, Matunga, Mumbai: 400019

ABSTRACT

Khadi fabric is the textile glummer of India and has been started to use in India from at least ten decades ago (from 1920s). Normally it consist of cotton, wool, silk like natural fibre etc. and the concern fabric is made by hand made (by charka spinning technology) yarn and in the traditional handloom process. Normally, different kind of natural dyes (vegetable based, wastage material based, tannin based colour) and the eco-friendly synthetic dyes are used for the coloration of the khadi textile. In addition some traditional printing techniques like hand screen printing, block printing is used for the special effect on the khadi textile. Concerning the value addition, only stiff khadi fabric is marketed which is made by adding starch. However, some special low cost other value addition of the khadi fabric will make it more acceptable to the consumers of the India and also in the other countries. In this respect, bioactive based finish and the mosquito repellent khadi textile is very much important. This kind of functionality will make the fabric hygienic in terms of attack by deadly mosquitoes and also some harmful microorganisms. Apart from it, if it is possible to make UV protective and the fire retardant khadi textile, it will increase its popularity and also gain the socio economic importancy to the consumers and the handloom weavers of India and the other subcontinental countries.

Keywords: *Khadi; Handloom; Dyein; Printing; Value addition*

1. Introduction

Khadi is a handspun, handwoven natural textile clothing using popularly in the various part of the India. Fibres like cotton, wool, silk are come into the domain of the khadi sector. Khadi, fabric (especially dhoti, shawls etc.,) has been used from the 1920s in different parts of the India and it is one of the integral part of the swadeshi movement in our country. Khadi movement initiated by the freedom fighter of India and has promoted the social, economical part of the Indian culture and also promoted the handloom weavers of India. Actually, in the British era, textile materials are very costly as they are value added from the outside country. First time Indian technology (by charka spinning) come into play and has made a soft, comfortable, cheap khadi fabric for the general peoples of India. It was popularised by different local names (Khaddar, tusar silk, puttapaka saree, Muslin etc.,) in the various part of the India. Khadi fabric is also marketed as the name of silk khadi, matka khadi, poly khadi and the Muslin Khadi. Therefore it can be considered as the cultural and the textile glummer of the India. Normally Khadi fabric is made of cotton yarn and it is porous, softer, fuller and comfortable to wear at the summer season. Additionally, most of the khadi fabric has lower cover factor as it is made of handmade yarn and in the handloom. Concerning the processing of the khadi fabric, normally it is dyed by different natural based colour. Moreover some other synthetic colour like reactive dye, direct dye, vat dye, acid and metal complex dyes are also have been used for the coloration of the khadi textile. Concerning printing, tie and dye, Batik printing and the "Damask printing" by using white print paste of the titanium di oxide and the natural based thickener are using popularly. For printing, hand screen and the block printing method was used normally. However, most of the printed khadi fabrics are heavy and coarse, may be due to the curing process it undergoes after printing and also suffer poor rubbing fastness property. Actually till date, no specific research or commercial work has been performed on the functionality of the khadi fabric. Here in this context a short plan on the value addition of the khadi

doi: 10.63019/ace.v1i2.584

fabric is discussed with its socio-economic importancy in the Indian market.

2. Dyeing and the Printing of the Khadi fabric

Most of the literature found in the concern area is related with the coloration and the printing of the khadi fabric. As far as the reported literature on the coloration (especially in dyeing) of the khadi fabric is concerned, different natural dyes extracted from turmeric (haldi), Babool chilka, Pomegranate peels (Anar chilka), Henna (Mehandi), Catachu (Katha), Madder (Majith), Indigo (Neel), Hararh, Marigold, Onions, Walnut Husks, etc. have been used for dyeing of the fabric along with different natural mordants like Alum, Copper Sulphate, Chrome, Tin, Oxalic Acid, Tartar, Acetic Acid, etc.,[Khadi india]. Some of the researchers also have been used extract of Nerium Oleander flower color [Dr. N. Vasugi Raaja], Cordia Sebestena flower [M. Kumaresan et.al.] etc., for the coloration of the khadi fabric. Apart from the natural dyeing of the khadi fabric, some of the synthetic dyes like vat dyes, reactive, sulphur and the metal complex dyes are also have been explored. In printing researcher applied azoic dyes and indigo by batik and tie dye printing method [Saranya et. al.]. Different printing style like patchwork, kantha, phulkare, block printing is very much popular in the printing area. Normally "Damask printing" is popular in the khadi sector which consist white print paste with 20-25% titanium di oxide (TiO_2) and guar gum thickener. Sometimes pigment colours are also added for colour printing effect. However, most of the printed khadi fabric are heavy, coarse and suffers poor rub fastness property. Additionally, no technical research has been reported on the value addition (adding functional property to the fabric) of the khadi fabric in the finishing stage. Concerning the value addition, only stiff khadi fabric is marketed which is made by adding starch.

3. Challenges of the Khadi fabric

From last few decades popularity of the Khadi textile gradually diminishes as many newer functional textile materials have emerges in the Indian market in low cost. Additionally, apart from the natural dyeing and the printing, the technology involved in the processing of the khadi fabric also not has been improved in that level so that it can be more popularise. Therefore for saving the ancient textile glummer of India and for the value addition of the khadi fabric some technical steps are mentioned in the following section.

4. Bioactive Khadi textile

Khadi, a porous permeable hand woven fabric (hand loom made fabric), made from hand spun yarn. Generally it is made from natural fibres like cotton, wool and silk. General aspect of the khadi fabric is it has lower cover factor (around 14) and the yarn of the fabric has less twist factor. Less twist factor helps in moisture absorbancy or permeable property of the fabric material. Most of the khadi fabric is fuller and voluminous in nature and normally used in summer season. Normally khadi garments have been used for the apparel purpose in the subcontinental countries like India. Here humidity and the temperature is the major concern of the environment. Therefore, there is ample chance of the microbes attack on the khadi apparel which results in smelling and swear degradation of fibres that's why anti-microbial finish (hygienic property) is an essential concern for the khadi fabric. Concerning the antimicrobial solution, different nano based compound like nano titanium di oxide, nano zinc oxide, nano alumina etc., can be explored for making the hygienic khadi textile.

5. Sun protective Khadi textile

Most of the marketed khadi fabrics are made of plain weave, lower ends and picks per inch (lower cover factor). Therefore there is high chance of the penetration of the UV rays (especially UVB and UVC) throughout the fabric. As a result end users of the khadi fabric may get affected by the adverse effect of the UV rays. However, due to the depletion of the ozone layer, from last few decades, majority of UV-B and UV-C are also reaching to earth and can easily transmitted through the lossely woven textile material. As a result person wearing cotton based khadi textile can easily affected by the harmful UV rays and there are strong chances of the cancer like deadly diseases. Therefore, in order to protect the end users of the khadi material from these harmful UV ray, sun protective finish is required. In this respect it

may be advantageous to use nano based titanium di oxide, zinc oxide etc., for the improvement of the sun protectiveness of the fabric.

6. Mosquito repellent khadi fabric

Normally khadi fabric has been used popularly in the India and the other asian countries. In all those countries the average temperature range is around 30-40°C with high humidity level. In this temperature and the humidity range is very much helpful for the reproduction of the mosquitoes. Additionally, khadi fabric is popular in the rural part of the India where more amount of the dense forests are exist. Apart from it, person wearing khadi fabric is sweated because of the heat and the humid condition of the environment. As a result of unmanageable forest existence, heat, humidity, sweat smell, mosquitoes are attracted to the end users. Recent market survey shows that the Dengue (disease occurred by mosquito bite) is the one of the most deadly disease in India. Therefore if the khadi fabric can be made mosquito repellent it will be more popularise in the rural market as well as in the urban sector. The concern fabric can be made mosquito repellent by using light oil based natural colour which consist aromatic smell and has potential to kill or restrict the mosquitoes. Some of the natural based promising examples are clove oil, citronella oil, eucalyptus oil, castor oil, nirgundi oil etc. All the aforementioned plants contain special aromatic molecule which is harmful for the nervous system of the mosquitoes. Additionally, these plants are easily available in the rural area of India and therefore rural people can easily made mosquito repellent khadi fabric by exploring those products.

7. Fire retardant based value addition of Khadi textile

Fire retardant is ananother important part of the value addition in the Khadi domain. Actually, most of the khadi fabric has been made by pure cotton and there is an ample chance of fire catch up in those fabrics. Therefore it will be very much helpful for the khadi customers if the concern fabric can be made fire retardant. Different fire retardant chemicals are available in the commercial market. However, they are costly and also not eco-friendly and after application the underlying textile materialturn stiffer and lost its aesthetic value. Additionally, lot of chemicals have been consumed for the desired fire resistant effect. Connected with this area, target is to improve the thermal stability of the khadi fabric by using eco-friendly chemicals like ammonium sulphamate, ammonium poly phosphate etc. These chemicals may be deposited on the fabric surface and will help in char mass formation by insulating effect. Apart from it some other products like di ammonium phosphate, urea, borax-boric acid mixture, alluminium tri hydrate, calcium carbonate etc., can be used for making fire retardant khadi fabric. It can save lot of life in the rural area of the India where khadi fabric is used popularly by the consumers.

8. Conclusion

As far as the reported literature is concerned, the dyeing (mainly natural dye, direct dye, metal complex, reactive dye used) and the printing area (mainly block printing, kantha, patchwork, phulkare techniques are used) of the khadi fabric have been well explored by the researchers, handloom sectors and the different textile industries. However, researches on the functionalities of the khadi fabric need to be explore further for the popularisation of the khadi textile in the India and also in the world market.

References

1. khadiindia.net/datafiles/user/Khadi%20Information.
2. Thesis of vasugi raja (Unpublished work).
3. Kumaresan M, Palanisamy PN, Kumar PE. Application of Eco-Friendly Natural Dye obtained from Cordia sebestena on Cotton using Combination of Mordants, J. Nat. Prod. Plant Resour, 2012; 2: 32-38.
4. Saranya R, Sheema CV, Asha TR, Designing and development of batik dyeing on khadi, International Journal of Applied science 2017; 2: 195-199.

Applied Chemical Engineering (2019) Volume 2 Issue 2
doi: 10.63019/ace.v1i2.586

Roentgenographic investigation of solid-phase equilibria in the PbSe-$AgSbSe_2$ system

Mansimova Shabnam Hamlet[1], Orujlu Elnur Najaf[2], Babanly Mahammad Baba[2]

[1] *Baku State University*

[2] *Institute of Catalysis and Inorganic Chemistry, ANAS, Baku*

ABSTRACT

The solid-phase equilibria in the 2PbSe-$AgSbSe_2$system were studied by using the powder X-ray diffraction method. It is established that the system is characterized by the formation of ~60 mol% solid solutions basedon $AgSbSe_2$.Solubility based on PbSe is about 3mol%. The cubic lattice parameters of solid solutions are defined.

Keywords: *silver-antimony selenide; lead selenide; solid solutions; powder X-ray diffraction; crystal lattice*

1. Introduction

Chalcogenides of heavy metals and their derivative phases are very attractive to the high-technologies thanks to their outstanding physical properties[1-3]. In particular, various materials such as Ag-B^V-Teand Ag-A^{IV}-B^V-Te(A^{IV}-Sn, Pb; B^V-Sb, Bi) alloys have high ZT valuesand are among the most promising thermoelectric materials[4-6]. Recent studies showed that some complex chalcogenidesof heavy p-metalsexhibit also topological surface states and can be used inspintronics and quantum computing[7,8]. In addition,silver chalcogenides and complex phases on their basis have mixed superion-electron conductivity and may beapplied in thermoelectric energy converters and differention-optical devices[9,10].

Optimization of functional properties of these materials can be achieved by changing their composition. This is based in turn on the study of systems consisted of structural analogs, since they can be expected to form wide regions of solid solutions[11, 12].

In this paper, we present the results of X-ray diffraction studies of solid-phase equilibria in the 2PbSe-$AgSbSe_2$ system.

Earlier we have studied some similar systems, in which new phases of variable composition were revealed:PbSe-$AgBiSe_2$[13], PbTe-$AgBiTe_2$ [14], SnTe-$AgSbTe_2$ [15], andSnTe-$AgBiTe_2$[16].

PbSeand$AgSbSe_2$ compounds crystallize in cubicNaClstructure(Sp.Gr.Fm3m) with lattice parameter: a=6.1243Å[17],a=5.786 Å[18], accordingly.

2. Experiments and results

The PbSe and $AgSbSe_2$compounds melt congruently at 1354 K[19] and 908 K[2]. Therefore, they crystallize from amelt of stoichiometric composition upon cooling. For the synthesis, the elementary components with a purity of at least 99.999% were used. Stoichiometric amounts of the starting components were put into silica tubesof about 20 cm in length and diameter of about 1.5 cm and sealed under a pressure of 10^{-2} Pa. $AgSbSe_2$wassynthesized by direct synthesis in a resistance furnace at 950 K followed by cooling in the switched-off furnace.PbSe was synthesized in a two-zone inclined furnace. The lower hot zone was heated to 1400 K, and the cold one to 900 K, which is somewhat lower than the boiling point of selenium[20]. The purity of the synthesized compounds was controlled by the XRD method by using the Bruker D8 diffractometer(CuK_α radiation), with a step size of 0.02°between 10°≤ 2θ ≤ 70°; data were collected at room temperature.The unit cell parameters of intermediate alloys were calculated by indexing of powder patterns using Topas V3.0 software. An accuracy of the crystal lattice parameters is shown in parentheses (Table).Crystallographic

doi: 10.63019/ace.v1i2.586

parameters of obtained compounds, practically almost coincide with the literature data[17, 18].

Compositions %$AgSbSe_2$	Phase compositions	Cubic lattice parameters, Å
0 (PbSe)	α	a=6.1246(5)
10	α+β	a=6.1184(6); a=6.0091(7)
20	α+β	a=6.1187(7); a=6.0101(7)
30	α+β	a=6.1185(6); a=6.0094(7)
40	β	a=5.9882(6)
60	β	a=5.9244(5)
80	β	a=5.8521(5)
100	β	a=5.7882(5)

Table 1. Phase compositions and crystallographic parameters of phases of the 2PbSe-$AgSbSe_2$ system

The alloys of the 2PbSe-$AgSbSe_2$ system were prepared by melting of the starting compounds in quartz ampules under vacuum followed by homogenizing annealing at 800 K (700 h).

In Fig.1, the powder X-ray diffraction patterns of some annealed alloys are presented. As can be seen, the diffraction patterns of alloys containing ≥40 mol% $AgSbSe_2$ are qualitatively similar to those for pure $AgSbSe_2$. X-ray diffraction patterns of alloys with compositions of 10, 20 and 30 mol% $AgSbSe_2$ consist of a set of diffraction lines of two cubic phases.

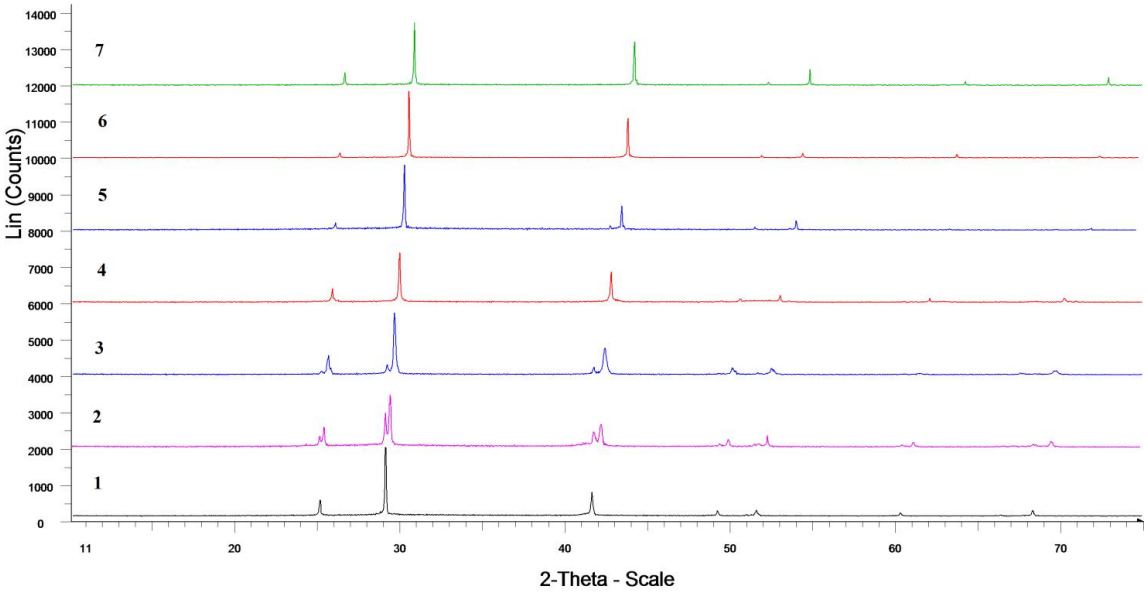

Рис.1. XRD powder patterns for starting compounds and some alloys of the 2PbSe-$AgSbSe_2$.

1-PbSe;2-10mol%; 3-30mol%; 4-40mol%; 5-60mol%; 6-80 mol%$AgSbSe_2$; 7-$AgSbSe_2$.

To determine the mutual solubility of the starting compounds in the studied system, we plotted the concentration dependences of the cubic lattices parameters (Table, Fig. 2). It is established that the dependencies have fracture points at compositions of 3 and 39 mol% AgSbSe2, which correspond to the limiting compositions of α- and β-solid solutions based on PbSe and AgSbSe2, respectively. It should be noted that in the α + β two-phase region, the lattice periods of the two coexisting phases have constant values regardless of the overall composition of the alloys, while

within the homogeneity region of the β phase the lattice period is a linear function of the composition, i.e. obey the Vegard's law.

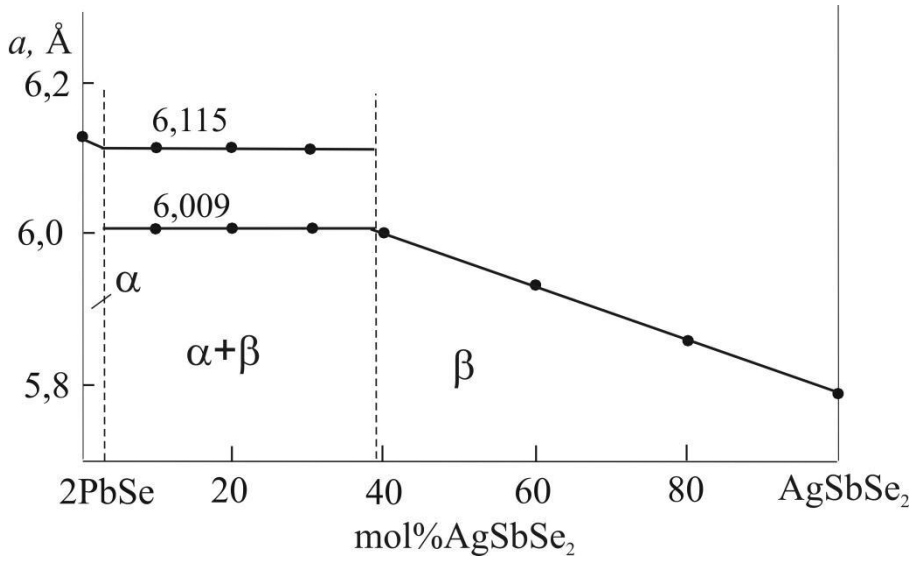

Fig.2: Concentration dependences of cubic lattices parameters.

The difference between studied system and above-mentioned [13-16] is that continuous series of high-temperature solid solutions were detected in them. The presence of a wide interval (3-39 mol% $AgSbSe_2$) of dissolution in the system 2PbSe-$AgSbSe_2$ (Fig. 2), is apparently associated with a large difference between the crystal lattices periods of the starting compounds.

3. Conclusion

Formation of a wide area of solid solutions based on $AgSbSe_2$ (40 mol%) is established in the 2PbSe-$AgSbSe_2$system based on the XRD results. The solubility based on PbSe is much lower and does not exceed 3 mol%. The crystal lattices parameters of the obtained solid solutions are determined.

Acknowledgment

The work has been carried out within the framework of the international joint research laboratory "Advanced Materials for Spintronics and Quantum Computing" (AMSQC) established between Institute of Catalysis and Inorganic Chemistry of ANAS (Azerbaijan) and Donostia International Physics Center (Basque Country, Spain).

References

1. Applications of Chalcogenides: S, Se, and Te, ed. by GurinderKaurAhluwalia, Springer, 2016.
2. Babanly MB, Yusibov YA, AbishevVT. Ternary Chalcogenide Based on Copper and Silver, BSU Publisher, 1993.
3. Babanly MB, Chulkov EV, Aliev ZS, *et al*. Phase diagrams in thematerials science of topological insulators based on metal chalcogenides. Russ. J. Inorg. Chem., 2017; 62(13): 1703 – 1729.
4. Shevelkov A.V. Chemical aspects of the design of thermoelectric materials. Russ. Chem. Rev., 2008; (77): 1-19.
5. Horichok I, Ahiska R, Freik D, *et al*. Phase Content and Thermoelectric Properties of Optimized Thermoelectric Structures Based on the Ag-Pb-Sb-Te System. J. Electron. Mater., 2016; 45(3): 1576-1583.
6. Kusz B, Miruszewski T, Bochentyn B, *et al*. Structure and Thermoelectric Properties of Te- Ag-Ge-Sb (TAGS) Materials Obtained by Reduction of Melted Oxide Substrates. J. Electron. Mater., 2016; 45(2): 1085-1093.
7. Papagno M, Eremeev S, Fujii J, *et al*. Multiple Coexisting Dirac Surface States in Three-Dimensional Topological Insulator PbBi6Te10. ACS Nano, 2016; 10(3): 3518-3524.
8. Shvets IA, Klimovskikh I.I., Aliev ZS, *et al*. Impact of stoichiometry and disorder on the electronic structure of the PbBi2Te4−xSex topological insulator. Phys. Rev. B, 2017; 235(96): 124 -7.
9. West A.R. Solid State Chemistry and its Applications, 2nd ed., Wiley, Hoboken, 2014.
10. Babanly MB, Yusibov YA, Babanly NB. The EMF Method with Solid-State Electrolyte in the Thermodynamic Investigation of Ternary Copper and Silver Chalcogenides. Electromotive Force and Measurement in Several Systems. S.Kara, Ed., Intechweb. Org, 2011; 57-78.
11. Villars P, Prince A, Okamoto H. Handbook of Ternary Alloy Phase Diagrams (10 volume set). American Technical

Publishers, 1995; 15000p.
12. Tomashik V, Feychuk P, Shcherbak L. Ternary alloys based on II-VI semiconductor compounds. Chernivtsi Books-XX1, 2010; 440 p.
13. Aliev I.I., Babanly KN, and Babanly NB. Solid Solutions in the Ag2Se-PbSe-Bi2Se3 System.Inorg. Mater., 2008; 44(11): 1179-1182.
14. Babanly NB, Aliev II., Babanly KN, *et al*. Phase Equilibria in the Ag2Te-PbTe-Bi2Te3 System. Russ. J. Inorg. Chem., 2011; 56(9): 1472-1477.
15. Mashadiyeva LF, Kevser JO, Aliev I.I., *et al*. Phase Equilibria in the Ag2Te-SnTe-Sb2Te3system and thermodynamic properties of the (2SnTe)1-x(AgSbTe2)xsolid solution. Phase equilibria and diffusion, 2017; 38(5): 603-614.
16. Mashadiyeva LF, Kevser JO, Aliev II, *et al*. The Ag2Te-SnTe-Bi2Te3 system and thermodynamic properties of the (2SnTe)1-x(AgBiTe2)x solid solutions series.J.Alloys. Compd., 2017; 724: 641-648.
17. DalvenR. A review of the semiconductor properties of PbTe, PbSe, PbS, and PbO. Infrared Phys., 1969; (9): 141-184.
18. Geller S., Wernick J. H.Ternary semiconducting compounds witch sodium chloride-like structure: AgSbSe2, AgSbTe2, AgBiS2, AgBiSe2. ActaCryst., 1959; (12): 46-52.
19. Massalski T.B., Ed., Binary Alloy Phase Diagrams, 2nd ed., ASM International, Materials Park, 1990; p 3589.
20. Emsley J. The elements, 3rd edition. Clarendon, Oxford University Press, 1998.

Applied Chemical Engineering (2019) Volume 2 Issue 2
doi: 10.24294/ace.v1i4.615

An overview to photo-catalytic degradation of dyes in waste water

Mohd. Hanief Najar[1], Ishtiyaq Ahmed Najar[2]

[1] Department of Chemistry, Govt. College of Engineering and Technology Safapora, Ganderbal-191201, J&K India
[2] Department of Environmental science, Govt. Degree College Ganderbal-191201, J&K India

ABSTRACT

Organic dyes used in textile and food industries are the important sources of environmental contaminations due to their non-bio degradability and high toxicity to aquatic creatures and carcinogenic effects on humans. This demands environmental remediation by the use of techniques which are environmentally benign. For this purpose, a general overview of dye degradation by light in the presence of materials as photo-catalysts has been given. The mechanism of action has also been described. Importantly, the materials involved in dye degradation usually involve nano-composites of either conducting polymers or metal-oxidesor graphene based systems which are insoluble in aqueous solutions, hence will be environmentally benign and can therefore be recovered after use.

Keywords: Nano-materials; Organic dyes; Photo-catalysis

1. Introduction and criteria for materials to be best photo-catalysts for dye degradation

The use of dyes in textile industries has become a serious environmental issue because of the unacceptable color of dye effluents, high chemical oxygen demand and resistance to bio-degradation on account of having complex aromatic structures. For this purpose, dyes in waste water are either removed by adsorption or degraded by photo-catalysis. In this area, semiconductor materials have attracted much attention. Among semiconductors, TiO_2 is considered a bench mark photo-catalyst for dye degradation. This is because of having high efficiency, low cost, chemical corrosion inertness, and long-term stability against photo-corrosion and chemical corrosion. Moreover, it is a photosensitive material, possesses high photo-catalytic activity, is stable in aqueous systems and has low environmental toxicity[1].But the major shortcoming to the use of TiO_2 photo-catalysts lies in having low quantum efficiency and the confined utilization of sunlight. For a material to exhibit high photo-catalytic activity, it must be porous and possess high surface to volume ratio so as to lead increased adsorption of dye. The high surface to volume ratio (surface area) can be attained provided the material to be either highly porous or nano-sized. This is the reason that benchmark TiO_2photo-catalyst has been found to be less efficient than nano-sized TiO_2.The material must exhibit slower recombination rate of photo-generated electron-hole pairs. This will help to cause facile degradation of dyes. ZnO was found to have almost same band gap energy as that of TiO_2, hence it was anticipated to be a better an alternative for TiO_2 photo-catalysts, but the fast recombination rate of photo-generated charge carriers limits its applicability. Reduction in the recombination rate can be attained by forming hetero-junctions between different components. This is indicative of making a composite material. However, this would demand the proximal interface contact. Moreover, materials with wider absorption range lead to enhanced efficiency in the degradation of dyes. For such a factor, TiO_2 again has limited applicability as it absorbs only a small portion of UV light. Thus to widen its absorption band spectrum, doping, composite science and the formation of hetero-junctions is essential. All the factors discussed above are complementary to one another. This we mean to say that a material with high surface to volume ratio does not suffice to be a good photo-catalyst unless other factors are more or less favoring. This demands the balance in the properties of materials desirable for photo-catalysis[2-5].

doi: 10.24294/ace.v1i4.615

2. Mechanism of Action and the development of systems

The mechanism of dye degradation involves the excitation of electrons from valence band (VB) to conduction band (CB) of the material by light irradiation. Due to this excitation, a vacancy is created in valence band called as hole. As the dye solutions are aqueous, holes produced in valence band trap water (H_2O) molecules to generate $^{\bullet}OH$ radicals while the electron in conduction band get trapped by the preadsorbed O_2 molecules thereby leading to superoxide ($O_2^{\bullet -}$) radicals which would react with protons to generate $^{\bullet}OH$ radicals. These radicals, since having strong oxidizing activity, then interact with dye molecules for causing their degradation into CO_2 and H_2O molecules which are environmentally benign[6].

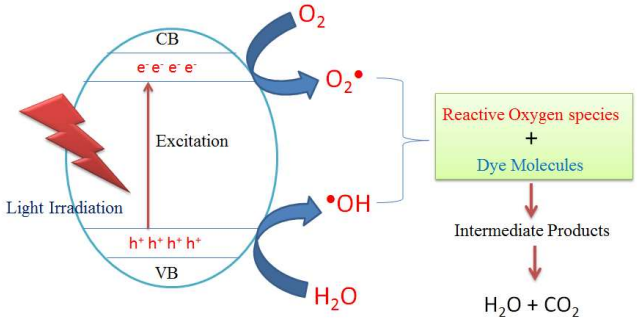

The presence of reactive oxygen species (ROS) for the degradation of dyes and hence the mechanism of degradation is normally proved by adding radical scavengers such as disodium salt of EDTA (EDTA-Na_2) and t-butyl alcohol. Their addition to the reaction mixture leads to the scavenging of such ROS thereby causinga reduced efficiency of dye degradation.

It has been observed that single walled titania (TiO_2) nanotubes are less efficient to cause dye (Methylene Blue) degradation under UV-light than double walled titania. This has been attributed to the greater surface area of later[7]. To enhance the separation of photo-induced charges and to reduce the rate of recombination, Bi_2O_3 has been coupled with $BaTiO_3$. The resulting hetero-junction was found to have an efficient interfacial contact, owing to which the photo-catalytic degradation of Rhodamine-B (RhB) has been enhanced to around 60% than pristine samples[8]. ZnO microspheres have been coupled with $CuInS_2$ and $CuInSe_2$. It has been observed that ZnO/$CuInS_2$ is having more photo-catalytic efficiency to degrade RhB dye as compared to ZnO/$CuInSe_2$ hetero-junction. This has been ascribed to the large surface area of former owing to small size. Moreover a high value of degradation efficiency has been achieved with ZnO/$CuInS_2$/$CuInSe_2$ system as shown in **Figure 1**. This is because of the formation of double hetero-junctions which lead to greater absorption of light and prevents effectively the recombination of electron-hole pairs[9].

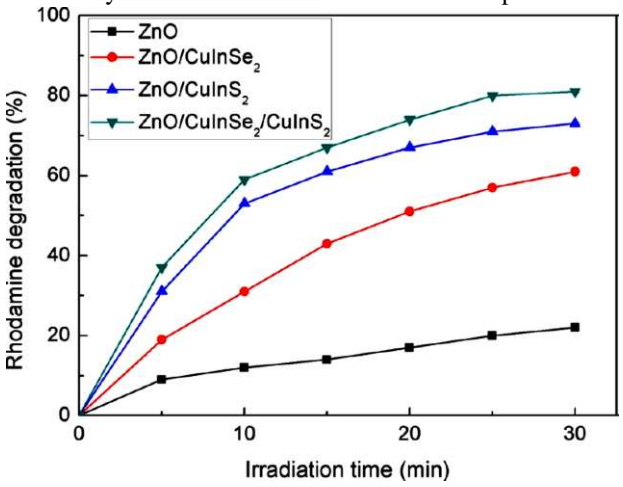

Figure 1. Photo-catalytic degradation kinetics of RB aqueous solution with an addition of ZnO microspheres, ZnO/$CuInSe_2$ (with mass ratio of 5:1) hetero-junction photo-catalyst, ZnO/$CuInSe_2$ (with mass ratio of 5:1) hetero-junction photo-catalyst, and ZnO/$CuInSe_2$/$CuInS_2$ (with mass ratio of 10:1:1) double hetero-junctions photo-catalyst.

In addition to the development of above hetero-junctions,conducting polymer based nanocomposite photo-catalysts have attracted much attention. For instance, many metal complexes form nano-composites with conducting polymers like polythiophene (PTh), Polyaniline (PANI) etc. PTh/$[Fe(CN)_3(NO)(bpy)]4H_2O$ nanocomposite fibers have been found to exhibit enhanced photo-catalytic activity. The main contributing factor for enhanced activity has been ascribed to the proximal interface contact as the surface area of such a sample has not impressed much. The proximal interface contact between $[Fe(CN)_3(NO)(bpy)]4H_2O$ and PTh has been justified by photoluminescence (PL) measurements. For the identification of ROS, scavangers like EDTA-Na_2 and t-butyl alcohol have been used that lead to reduced methyl orange (MO) dye degradation as

shown in **Figure 2**[10].

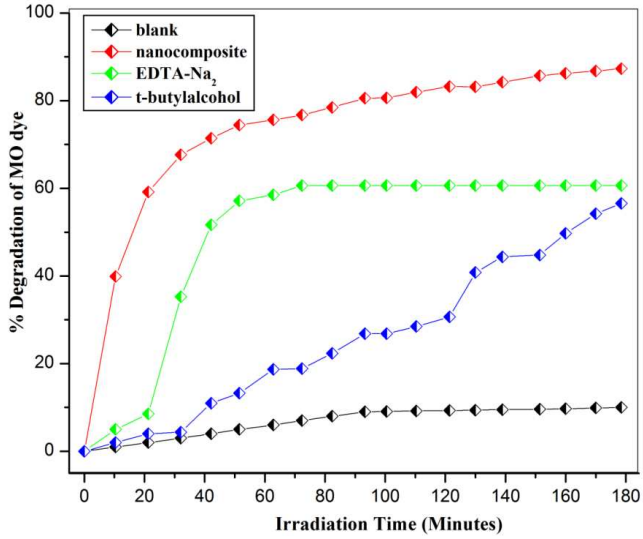

Figure 2. Dye degradation of nanocomposite and nanocomposite in the presence of scavengers

3. Conclusion

Water treatment is a necessity inorder to minimize the scarcity of water and to avoid environmental contamination from the textile industries. The understanding of eco-friendly materials as photo-catalysts by which environmental remediation can occur has been assessed. The factors responsible for the enhancement or reduction in the degradation of dyes have been taken into consideration.

References

1. Pan Xiong, Lianjun Wang, Xiaoqiang Sun,Binhai, Xuand Xin Wang. Ternary Titania−Cobalt Ferrite−Polyaniline Nanocomposite: A Magnetically Recyclable Hybrid for Adsorption andPhotodegradation of Dyes under Visible Light, Ind. Eng. Chem. Res 2013; 52: 10105−10113.
2. Chen C., Lu C., Chung Y. Photocatalytic degradation of ethyl violet in aqueous solution mediated by

ch, RSC Adv 2015; 5: 107209–107221.

TiO2 suspensions,J. Photochem.Photobiol., A: Chem 2006; 181: 120−125.

3. Oliveira A. S., Saggioro E. M., Barbosa N. R., Mazzei A., Ferreira L. F. V., Moreira J. C. Surface-photocatalysis: A study of the thickness of TiO_2 layers on the photocatalytic decomposition of soluble indigo blue dye, Rev. Chim. (Bucharest, Rom.) 2011; 62: 462−468.
4. Sojić D., Despotović V., Abramović B., Todorova N., Giannakopoulou T., Trapalis C.. Photocatalytic degradation of mecoprop and clopyralid in aqueous suspensions of nanostructured N-doped TiO_2, Molecules 2010; 15: 2994−3009.
5. Vasapollo G., Mele G., Sole R. D., Pio I., Li J., Mazzetto S. E.. Use of novel cardanol-porphyrin hybrids and their TiO_2-based composites for the photodegradation of 4-nitrophenol in water, Molecules 2011; 16: 5769−5784.
6. M. HasmathFarzana, SankaranMeenakshi. Synergistic Effect of Chitosan and Titanium Dioxide on the Removal of Toxic Dyes by the Photodegradation Technique. Ind. Eng. Chem. Re. 2014; 53: 55−63.
7. Kun Liang, Beng Kang Tay, Olga V. Kupreeva, Taisiya I. Orekhovskaya, Sergei K. Lazarouk, Victor E. Borisenko. Fabrication of Double-Walled Titania Nanotubes and Their Photocatalytic Activity. ACS Sustainable Chem. Eng 2014; 2: 991−995.
8. Haimei Fan, Haiyan Li, Bingkun Liu, Yongchun Lu, TengfengXie, Dejun Wang. Photoinduced Charge Transfer Properties and Photocatalytic Activity in $Bi_2O_3/BaTiO_3$ Composite Photocatalyst, ACS Appl. Mater. Interfaces 2012; 4: 4853−4857.
9. FengyuShen, WenxiuQue, Yucheng He, Yuan Yuan, Xingtian Yin and Gangfeng Wang. Enhanced Photocatalytic Activity of ZnO Microspheres via Hybridization with $CuInSe_2$ and $CuInS_2$Nanocrystals, ACS Appl. Mater. Interfaces 2012; 4: 4087−4092.
10. Mohd Hanief Najar, Kowsar Majid. Enhanced photocatalytic activity exhibited by PTh/ $[Fe(CN)_3(NO)(bpy)]4H_2O$ nanocomposite fibers viaa synergistic approa

Applied Chemical Engineering (2019) Volume 2 Issue 2
doi:10.24294/ace.v1i2.428

Study on Phase Transformation and Desulfurization Ability during Refining with Flux Additions of B_2O_3 and CaF_2 into CaO-Based Desulfurizer

Chih-Chun Hsieh[1*], Cheng-Han Wu[2], Weite Wu[2*]

[1] Department of Materials Science and Engineering, National Chung Hsing University, Address: No.1, Julun Rd., Gangshan Dist., Kaohsiung City 820, Taiwan. E-mail: jeromehsieh@gmail.com

[2] Department of Materials Science and Engineering, National Chung Hsing University, 250 Kuo-Kuang Rd., Taichung 402, Taiwan. E-mail: wwu@nchu.edu.tw

ABSTRACT

CaF_2 aids melting and desulfurization, but can also cause environmental pollution. Thus, it has become important to discuss the phase transformation and find a substitute for CaF_2. A CaO-based desulfurizer with various flux additions of B_2O_3 and CaF_2 is investigated during the refining process. The purpose of this study is to discuss the phase transformation and desulfurization ability and during refining with B_2O_3 and CaF_2 using a high frequency furnace. Experimental results indicate that the melting temperature of CaO-Al_2O_3-SiO_2 series desulfurizer becomes lower when more B_2O_3 and less CaF_2 are added. On the other hand, the desulfurization ability can be affected within 15 min when various proportions of B_2O_3 and CaF_2 are added. The desulfurization ability is better with a high content of B_2O_3 desulfurizer within a 15 min period. However, the desulfurization ability is not affected by the proportion of B_2O_3 and CaF_2 for a long melting period (30 min).

Keywords: Compounds; Oxides; Recycling; Phase Transformation; X-Ray Diffraction

1. Introduction

In recent years, some steel companies' use of arc furnace steel-making processes has grown rapidly, leading to an increasing demand for scrap steel. It is difficult to produce high-quality steel with arc furnace steel-making, because the scrap steel contains large amounts of impurities. Therefore, the refining process in arc furnace steel-making is very important.

The ladle furnace (LF) technique not only easily adjusts to the temperature of the molten steel, but also randomly increases various alloy elements or compounds. Therefore, the ladle furnace is the most commonly used equipment for refining molten steel[1-2]. Great amounts of desulfurization slag are produced after refining desulfurization. Most steel plants discard this desulfurization slag, resulting in industrial cost and environmental pollution; the recycling of the desulfurization slag can reduce environmental pollution.

Many recent investigations have focused on the recycling of desulfurization slag. According to these papers[3-6], the desulfurization slag has been partly applied to the raw materials of cement, road repair and construction, due to the stability of its physical and chemical properties and nontoxic characteristics. Some researches[7-9] have also pointed out that desulfurization slag contains residual Free-CaO. Therefore, it is worth discussing the effect of recycling desulfurization slag on the sulfur content of molten steel.

Hino et al.[10] have confirmed that the effectiveness of desulfurization flux is related to its chemical composition. In a CaO-Al_2O_3-MgO ternary slag system, the desulfurization ability is proportional to the CaO/MgO at the constant of Al_2O_3. The decay of the desulfurization ability is attributed to the increscent of

doi: 10.24294/ace.v1i2.428

SiO_2 and Al_2O_3 in a CaO-SiO_2-Al_2O_3 ternary slag system. Furthermore, a few researches have focused on recycling desulfurization slag.

Regarding the compositional design of the desulfurizer, both a high CaO content and a low melting point are desired, but very difficult to achieve. Therefore, the addition of flux into a desulfurizer is necessary during the refining process. The flux additions have two advantages: (1) decreasing the melting point, and (2) accelerating the desulfurization reaction. CaF_2 flux is often used in desulfurizers because of its good desulfurization effect. However, the addition of CaF_2 corrodes the refractory of the furnace liner, decreasing desulfurization efficiency. Also, toxic gas will be released when the CaF_2 flux is used, and may harm many people, animals and plants[5]. As described above, finding a substitute for CaF_2 is very important for ecological protection.

The purpose of this study is to discuss the desulfurization ability during refining with the addition of two fluxes: B_2O_3 and CaF_2, into a CaO-based desulfurizer. The substitution of B_2O_3 for CaF_2 is also discussed in terms of melting point and desulfurization ability.

2. Experimental procedures

Low carbon steels (S15C) with a specific weight of 500 g was selected as the experimental material and placed in a high frequency furnace crucible. Then, 0.685 g FeS was added to increase the S content of the molten steel. After the FeS is melted, Al bars (2.1g) were placed in a high frequency furnace crucible for deoxidation, with the main purpose being to decrease the partial pressure of the oxygen of the molten steel. This procedure can enhance desulfurization. Finally, some compositions of desulfurizer (CaO, Al_2O_3, SiO_2, MgO, CaF_2, and B_2O_3) were placed in a high frequency furnace crucible. The reaction times of desulfurization were 15 and 30 min. In this study, experimental analyses can be divided into slag analysis, steel analysis and refractory analysis.

After melting, the slag and steel ingots were analyzed. For the slag analysis, the phase identification was examined using an XRD (SIEMENS D5000), and composition was analyzed using an XRF (PANalytical PW2640), a C/S analyzer (Leco CS230) and a wet chemical analytical technique. The chemical composition of the steel ingots was performed using a spark discharge spectrometer (Oxford ARC-MET8000).

In this study, desulfurization was studied with a CaO-based desulfurizer, the composition of which was designed according to the CaO-Al_2O_3-SiO_2 ternary phase diagram (**Figure 1**[11]). A lower melting point and higher CaO content were considered in order to satisfy the condition of desulfurization. Therefore, the based composition of desulfurizer (55%CaO-35%Al_2O_3-10%SiO) was used in this study. On the other hand, 8% MgO was added to replace the 8% Al_2O_3 in order to protect the refractory of the furnace liner.

The compositions of desulfurizer can be divided into five groups (A~E). The compositions of A~B groups were 59.78%CaO-20.65%Al_2O_3-10.87SiO_2-8.69MgO and 55%CaO-19%Al_2O_3-10SiO_2-8%MgO-8% CaF_2. The groups of C~E had 2% B_2O_3, 5% B_2O_3, and 8% B_2O_3 added, respectively, and 2% CaF_2, 5% CaF_2, and 8% CaF_2 reduced, respectively. Detailed compositions of the A~E groups are listed in **Table 1**. The melting points of desulfurizers for the five groups are examined using a TGA/DTA simultaneous thermal analyzer (LINSEIS STA PT1600).

3. Results and discussion

3.1 Melting point examination of desulfurizer

The melting points of A~E groups can be analyzed using a TGA/DTA simultaneous thermal analyzer. **Figure 2** shows the DTA thermal analysis results of the five groups. An endothermic peak was detected between 450 ^oC and 480 ^oC, and this peak was a reaction peak of water of crystallization of CaO. However, another endothermic peak was also observed at a temperature range from 1245 ^oC to 1404 ^oC, and this repre-

Figure 1. CaO-Al_2O_3-SiO_2 ternary phase diagram.

Specimen	Content of compound (wt.%)					
	CaO	**Al_2O_3**	**SiO_2**	**MgO**	**CaF_2**	**B_2O_3**
A	59.78	20.65	10.87	8.69	0	0
B	55	19	10	8	8	0
C	55	19	10	8	6	2
D	55	19	10	8	3	5
E	55	19	10	8	0	8

Table 1. Chemical composition of desulfurizer

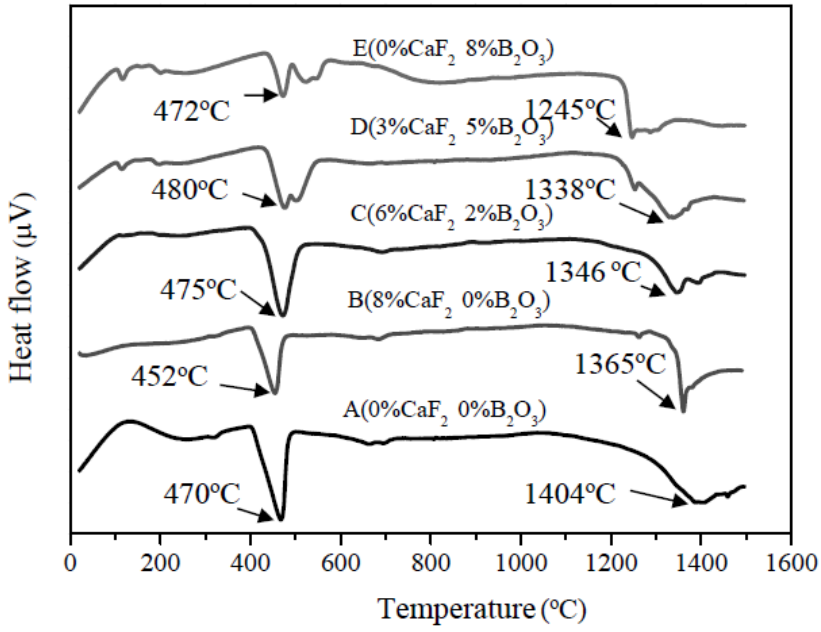

Figure 2. Thermal analyzed results of desulfurizers.

sented the melting points of desulfurizer for the five groups. Furthermore, the melting points had decreasing tendencies for desulfurizers of groups A~E. The melting points decreased from 1,404 °C to 1,245 °C when B_2O_3 contents increased from 0% to 8%. In regard to the melting point, the B_2O_3 can replace the CaF_2, and is a better flux in desulfurization than CaF, because B_2O_3, CaO, Al_2O_3, and MgO can form low melting point eutectic compounds. The CaF_2 and Al_2O_3 MgO can also form low melting point compounds, but the melting point of eutectic compound in B_2O_3 is lower than that in CaF_2. As stated above, the melting point of the desulfurizer can be decreased to 1245 °C.

3.2 Compositional analysis of steel ingot

The chemical compositions and desulfurization ratios of steel ingots after 15 and 30 min of melting times are shown in **Tables 2** and **3**, and **Figure 3**. It indicates that the desulfurization ratio has no obvious change after 30 min. However, the desulfurization ratio exhibits a variation after 15 min. The desulfurization ratio of group A without a flux addition is lower after 15 min than other desulfurization ratios of groups B~E. However, other desulfurization ratios of groups B~E are very close, which means that the flux additions can promote the desulfurization ability within a short time. On the other hand, the desulfurization ratio of group A can be increased to 12.4%, while those of groups B~E can only be raised to 5~7% after 15 min; this means that group A does not show excellent desulfurization ability within 15 min. Furthermore, groups B~E indicate better desulfurization ability within 15 min, so the increment of desulfurization ratios is limited over 15 min.

Groups	Content of compound (wt.%) (15 min)									
	CaO	F-CaO	Al_2O_3	SiO_2	MgO	MnO	C	S	B	T-Fe
A	22.489	0.086	22.458	33.562	3.616	16.903	0.028	0.039	0.009	1.119
B	20.017	0.059	23.293	36.281	3.578	16.556	0.030	0.050	0.018	1.056
C	21.879	0.061	29.492	34.475	3.968	15.742	0.027	0.049	0.152	1.026
D	19.924	0.057	25.781	34.063	3.324	14.802	0.026	0.052	0.320	1.217
E	23.252	0.057	21.205	33.871	3.425	13.181	0.021	0.050	0.523	1.033

Table 2. Chemical composition of slag at 15 min

Groups	Content of compound (wt.%) (30 min)									
	CaO	F-CaO	Al_2O_3	SiO_2	MgO	MnO	C	S	B	T-Fe
A	19.591	0.059	17.705	39.362	2.796	16.188	0.027	0.054	0.012	1.135
B	18.129	0.043	19.258	41.930	2.396	17.804	0.029	0.055	0.008	1.141
C	23.105	0.040	17.934	41.190	3.358	12.320	0.027	0.055	0.124	1.284
D	21.857	0.037	18.337	40.450	3.042	14.182	0.025	0.058	0.295	1.004
E	20.604	0.038	21.585	39.600	3.031	14.550	0.022	0.059	0.508	1.177

Table 3. Chemical composition of slag at 30 min

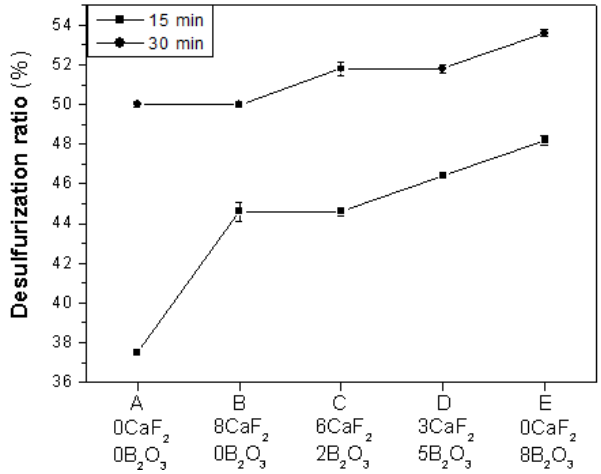

Figure 3. Relationship between the desulfurization ratios and desulfurizers at 15 min and 30 min.

The desulfurization ratios of groups B~E with flux additions of B_2O_3 and CaF_2 show no obvious change. However, the desulfurization ratios of higher B_2O_3 content (groups D~E) after 15 min melting were higher than that of lower B_2O_3 content (groups A~C). This result indicates that the B_2O_3 flux additions can increase the desulfurization ability within 15 min, and shrink the difference of desulfurization ratios between 15 and 30 min. This means that the desulfurization reaction is almost finished after 15 min, so the desulfurization reaction time can be increased. Therefore, B_2O_3 can substitute CaF_2 for improving desulfurization.

3.3 Compositional analysis of slags

The compositions and the S contents of slags after 15 and 30 min of melting are shown in **Figure 4**. The S content in group A is lower than groups B~E because the flux does not help the rapid dissolution of CaO after 15 min of melting. However, the S contents are very close with flux additions after 15 and 30 min of melting. This is because the fluxes can improve the rapid dissolution of CaO. Groups B~E display good desulfurization ability after 15 min of melting. Therefore, the desulfurization ability in slag will be limited over 15 min of melting. The difference of S contents becomes very small when the contents of B_2O_3 are higher (groups D~E).

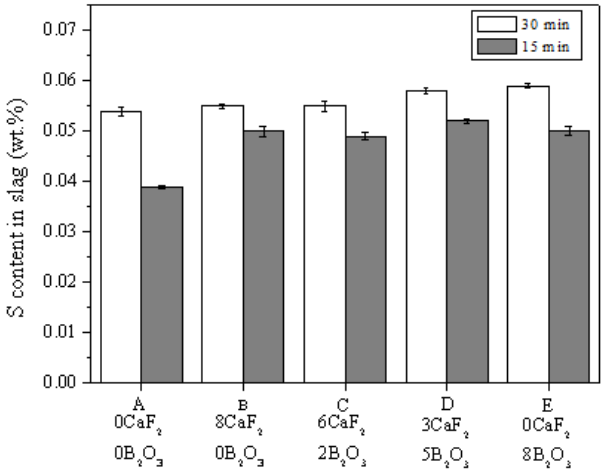

Figure 4. Relationship between the S contents in slag and desulfurizers at 15 min and 30 min.

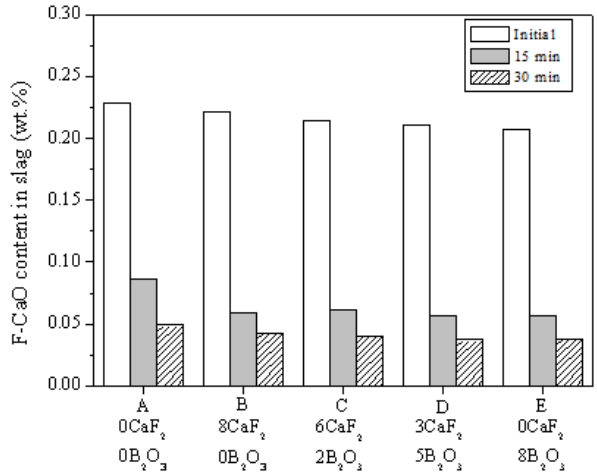

Figure 5. Relationship between the Free-CaO in slag and desulfurizers at 15 min and 30 min.

Figure 5 shows the Free-CaO contents in slag with different melting times. The contents of Free-CaO without flux addition are higher than that with flux addition after 15 and 30 min because a lot of unreacted CaO is present without a flux addition and the desulfurization reaction does not proceed adequately in the

desulfurizer. However, there are lower Free-CaO contents in groups B~E than in group A. Less unreacted CaO is present in groups B~E, so the desulfurization reaction can be completed. The desulfurization has a similar effect with flux additions of B_2O_3 and CaF_2 after 15 and 30 min. However, the desulfurization effect of B_2O_3 is better than that of CaF_2. Hence, the B_2O_3 promotes the rapid desulfurization of CaO.

3.4 Relationship between desulfurization ratio and Free-CaO content

Figure 6 combines **Figures 3** and **5**. The relationship between the desulfurization ratio of a steel ingot and the amount of Free-CaO slag is shown in **Figure 6**; it shows that the desulfurization ratio of the steel ingot and amount of CaO slag have a linear relationship, and their correlation can be represented as Equation (1). The desulfurization ratio can be increased when the used amount of CaO is increased. This means that the desulfurization ability can be improved when higher Free-CaO contents are consumed during the desulfurization. Therefore, Free-CaO is an important compound for the desulfurization reaction.

$$\text{Desulfurization ratio (\%)} = 0.7135 + 286.96[\text{F-CaO(wt.\%)}] \quad (1)$$

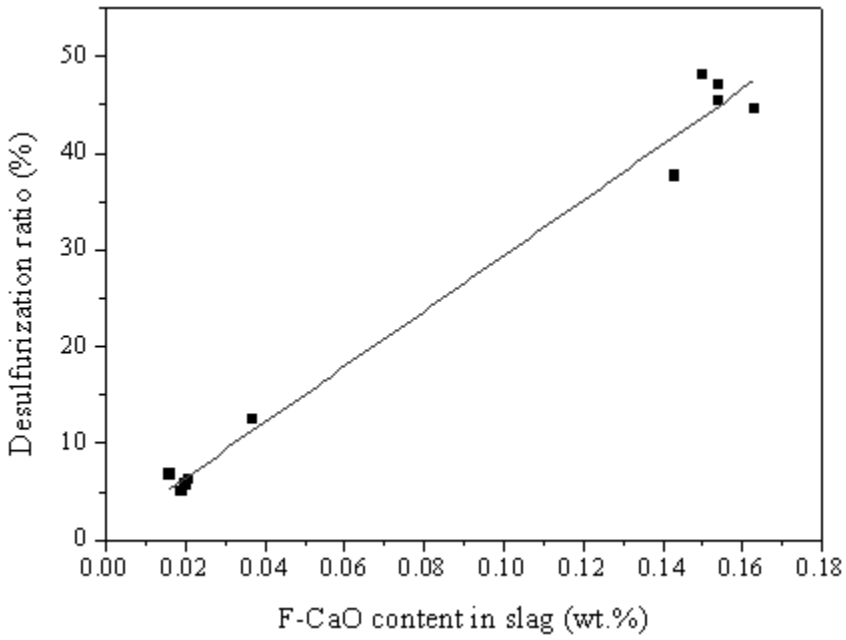

Figure 6. Relationship between the desulfurization ratios and Free-CaO contents.

3.5 Phase transformation of CaO-CaF2 and CaO-B2O3 at high temperature

The CaO-B_2O_3 (1:1) was mixed and heated to 1,650 ^oC with a heating rate of 5 ^oC/min via a high temperature furnace in order to understand the fluxing mechanism of CaO under high temperature. Following this, the high temperature compounds were analyzed using the XRD.

Figure 7 shows the compounds of the CaO and CaF_2; no new precipitate was found after heating. Hence, the fluxing mechanism of CaO did not result from the precipitation of low melting point compounds. The diffraction peaks of the $CaAl_2O_4$ and $CaAl_4O_7$ compounds were detected, with two peaks derived from the Al_2O_3 crucible.

In **Figure 8**, the diffraction peaks of $Ca_2B_2O_5$ were examined; this compound was a low melting point compound[12]. The compounds of $Ca_2B_2O_5$ can help with the rapid dissolution of CaO during melting as well as to achieve a fluxing effect. Therefore, the desulfurization reaction can also be accelerated. It can be proven that the addition of B_2O_3 and CaO into the desulfurizer can be reacted as a compound of low melting point, $Ca_2B_2O_5$. Similarly, the diffraction peaks of $CaAl_2B_2O_7$ and Al_2O_3 were also derived from the Al_2O_3 crucible.

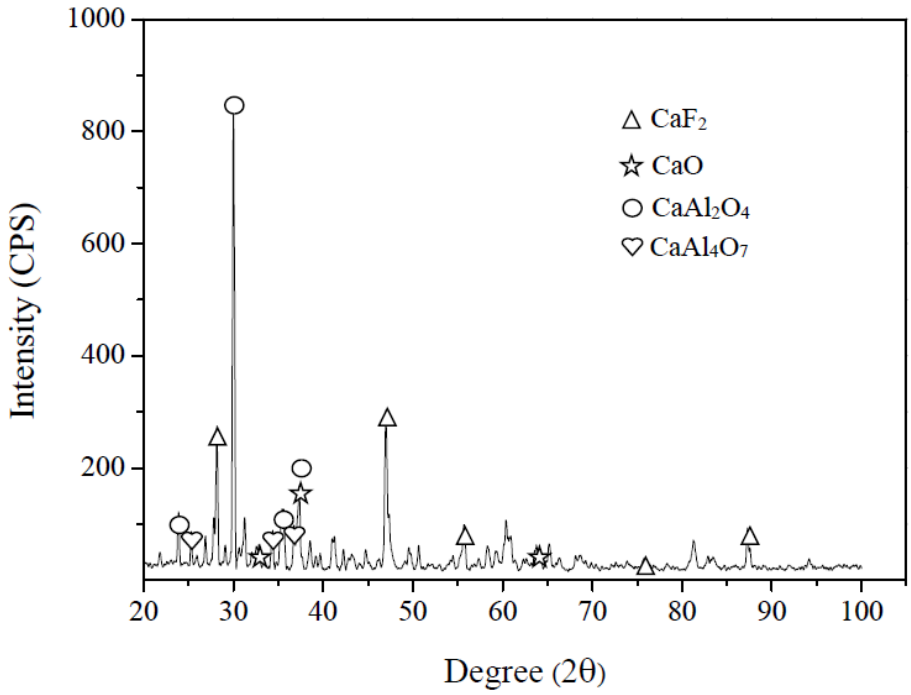

Figure 7. XRD diffraction pattern of CaO-CaF_2.

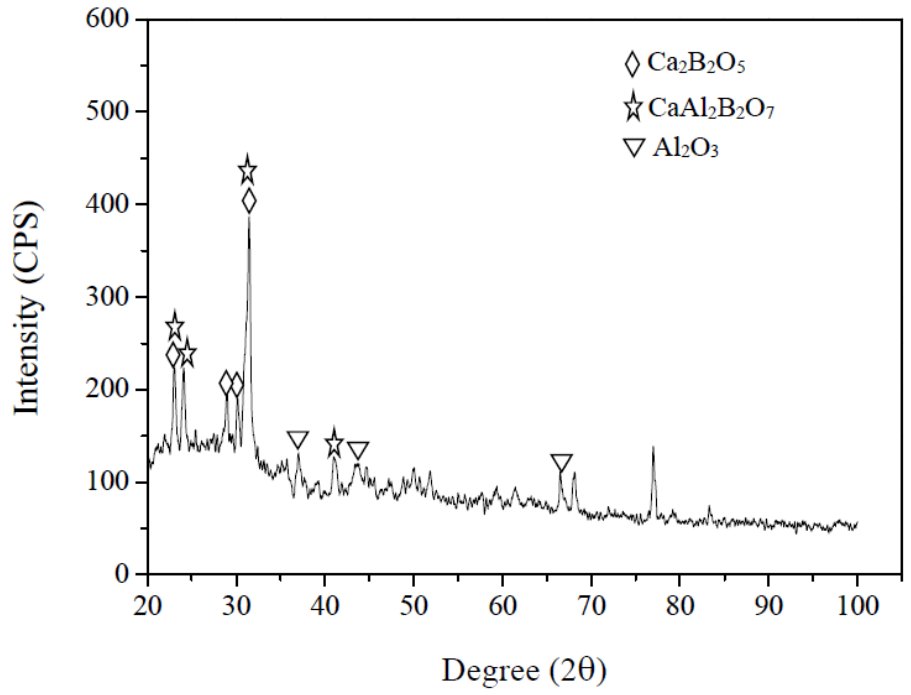

Figure 8. XRD diffraction pattern of CaO-B_2O_3.

4. Conclusions

This study discusses the phase transformation and desulfurization ability for a CaO-based desulfurizer with different flux contents of CaF_2 and B_2O_3. Some significant results can be summarized as follows:

1) In the CaO-based desulfurizer, the CaF_2 content is lower when the B_2O_3 content is higher, which leads to a lower desulfurizer melting point, especially with 8% B_2O_3. The desulfurizer melting point (8% B_2O_3) was the lowest of all contents.

2) Different ratios of CaF_2 and B_2O_3 can affect the desulfurization ability within a short time, and the desulfurizer (8% B_2O_3) shows excellent desulfurization ability within a short time.

3) The desulfurization ability of CaO-based desulfurizer is not affected by CaF_2 and B_2O_3 contents for a long desulfurization time, but the Free-CaO can dominate the desulfurization ability of the CaO-based desulfurizer.

4) A linear relationship between the desulfurization ability of the CaO-based desulfurizer and the Free-CaO content of the desulfurizer exists as follows: Desulfurization ratio (%) = 0.7135 + 286.96 [Free-CaO (wt.%)].

Conflict of interest

The authors declared no conflict of interest.

Acknowledgements

The authors are obligated to thank the National Science Council of the Taiwan, R.O.C. for the financial support under the projects numbered NSC 100-ET-E-005-001-ET, NSC 100-2811-E-005-001, and 100-EC-17-A-08-S1-117.

References

1. Wang H, Li G, Li B, *et al.* Effect of B2O3 on melting temperature of CaO-based ladle refining slag. Journal of Iron and Steel Research International 2010; 17(10): 18–22.
2. Hong X, Zheng Q, Jiang G, *et al.* In: Kanagy DI (editor). Proceeding of 84th Steelmaking Conference; 2001 Mar 25–28; Baltimore, Maiyland. Association for Iron & Steel Technology; 2001. p. 715.
3. Chen YL, Chang JE, Shih PH, *et al.* Reusing pretreated desulfurization slag to improve clinkerization and clinker grindability for energy conservation in cement manufacture. Journal of Environmental Management 2010; 91(9): 1892–1897.
4. El-Mahllawy MS. Characteristics of acid resisting bricks made from quarry residues and waste steel slag. Construction and Building Materials 2008; 22(8): 1887–1896.
5. Durinck D, Engström F, Arnout S, *et al.* Hot stage processing of metallurgical slags. Resources, Conservation and Recycling 2008; 52(10): 1121–1131.
6. Kuo YM, Huang KL, Wang CT, *et al.* Effect of Al_2O_3 mole fraction and cooling method on vitrification of an artificial hazardous material. Part 1: Variation of crystalline phases and slag structures. Journal of Hazardous Materials 2009 169(1–3): 626–634.
7. Das B, Prakash S, Reddy PSR, *et al.* An overview of utilization of slag and sludge from steel industries. Resources, Conservation and Recycling 2007; 50(1): 40–57.
8. Li HJ, Suito H, Tokuda M. Proc. 1st. Int. Conf. on Processing Materials for Properties, 1993. ISIJ international 1995; 35(9): 1079–1088.
9. Nakai Y, Kikuchi N, Iwasa M, *et al.* Development of slag recycling process in hot metal desulfurization with mechanical stirring. Steel Research International 2009; 80(10): 727–732.
10. Hino M, Kitagawa S, Ban-Ya S. Sulphide capacities of CaO-Al_2O_3-SiO_2Slags. Tetsu-to-Hagané 1993; 79(1): 34–40.
11. Sutcu M, Akkurt S. Utilization of recycled paper processing residues and clay of different sources for the production of porous anorthite ceramics. Journal of the European Ceramic Society 2010; 30(8): 1785–1793.
12. Yu X, Shi Q, Zhai R, *et al.* Influence of B2O3 on melting haracteristics of CaO-Al2O3-SiO2-MgO-CaF2 pentary slag series. Special Steel 2006; 27(4): 5–7.

Applied Chemical Engineering (2019) Volume 2 Issue 2
doi: 10.24294/ace.v1i2.432

Validation of Flory-Huggins Model for Phenol Adsorption by Parthenium Hysterophorus in A Batch System

Zakia Latif[1], Aliya Fazal[2], Muhammad Aziz Choudhary[1], Zahoor Ahmad[1], Muhammad Aslam Mirza[1]

[1] Department of Chemistry, Mirpur University of Science& Technology (MUST), Mirpur,10250 AJ&K, Pakistan
[2] National centre for physics, Quaid-e-Azam University campus, Islamabad, 44000 Pakistan,

ABSTRACT

Parthenium hysterophorus weed powder was studied as adsorbent for phenol adsorption from its aqueous standardized solution. The adsorption of pollutant was found improving with an increase of biomass dosage and contact time. The intraparticle diffusion of phenol onto adsorbent surface was identified to be the rate limiting step. Linear form of Flory-Huggins model revealed preeminence to Langmuir, Freundlich, Temkin, and Dubinin-Radushkevich due to highest value of R^2. The remediation process was figured out as a physisorption rather than a chemical one based on value of E (0.21KJ/mol). Active sites of sorbent surface identified by FT-IR were oxygen containing functional groups. Recent study proposes cost effective utilization of toxic allergent for treatment of toxic waste.

Keywords: Adsorption; Kinetic; Equilibrium; Active sites

1. Introduction

Against the principles of sustainable development, unrestrained industrial practices resulted undesirable rich levels of injurious and toxic substances in the environmental media. Industrial waste matter is often polluted with different compounds such as: metallic element, pendent solids, and dissolved organic compounds[1]. Among these xenobiotic phenol treatment is explored due to its release from major material and pharmaceutical industries, petrochemical industries, petroleum refineries, coal gasification operations, textiles, iron, steel, pulp and paper, plastic, rubber, and pesticides[2,3]. Phenol contaminated water remediation is necessary before discharge into natural water because they are classified as hazardous wastes and some are known or suspected as carcinogens. Environmental Protection Agency (EPA) has set a limit of phenol 0.1 mg/L in wastewater and 0.001 mg/L in potable water by The World Health Organization (WHO).

The existing problem of organic contaminant is resistance to decompose organically, opposes the self-purification capabilities of the rivers as well as remediation in conventional wastewater treatment plants[4]. Among the physicochemical processes that have proved useful for phenol treatment adsorption is particularly important due to its sludge free neat operation, economical, handiness of wide range of adsorbents and complete dismissal of phenols from wastewaters. Many agricultural wastes have been employed as adsorbent for the removal of phenol includes coconut shell[5], sawdust[6], apricot stone shell[7], sugarcane bagasse[8], peanut husk[9], coir pith and rice husk[10]. Present study is about use of Parthenium hysterophorous as adsorbent for remediation of phenol. Parthenium hysterophorous a poisonous and conceivable weed scatters quickly in waste and grazing land. In addition to allelopathic effect, number of human health problems like skin allergy, dermatitis and irritation to eyes is reported for this weed. Similarly it is indigestible and harmful to domestic animals and causes food shortage[11]. Considering its harmful effects it is selected to test phenol decontamination as a strategy to sort solution at two levels.

2. Experimental

2.1 Sample collection, preparation and characterization

Parthenium hysterophorous (PH) weed was collected from Margallah Hills Islamabad in the month of June (2013),

doi: 10.24294/ace.v1i2.432

weed was fresh and green at the time of sampling therefore to reduce water content it was sun-dried for about 5-6 days. The dried sample was crushed in a ball mill/grinder and passed through US standard sieve (mesh No. 80 mm) to obtain particle size of 180µm. Sieved samples were stored separately in polyethene bags to prevent readsorption of moisture before Phenol sorption. The surface functionality of samples was analyzed by FTIR spectrum (FTIR-8400, Shimadzu, Japan) in the wave number range of 4000-500cm^{-1}. The dried powder was ground with KBr (AR grade) at a ratio of roughly 1/1000. 500 mg of mass was made in to a pellet by pressing at 80KN for 1 min. After preparation, the pellet was analyzed immediately, and the spectra were recorded to 4cm^{-1} resolution. Surface morphology of biomass was observed by scanning electron microscopy ((SEM, JEOL model JSM-6490-A, Japan) at different magnifications.

2.2 Solutions and standardization

Reagents employed for batch biosorption study of Phenols are Chloroform, hydrochloric acid (conc.), potassium iodide (solid crystals), sulphuric acid (1N), standard sodium thiosulphate (0.025N), ammonium hydroxide (0.5N), starch (2g) dispersed in 100ml distilled water and methyl orange indicator (0.05ml dissolved in 100ml of distilled water). Bromate- bromide solution was prepared by dissolving anhydrous $KBrO_3$ (0.2784 g) in distilled water, to which 1g KBr crystals were added and diluted to 100mL. Phosphate buffer was prepared by dissolving potassium mono hydrogen phosphate (10.45 g) and potassium di-hydrogen phosphate (7.23 g) in 100mL of distilled water maintaining pH of solution at 6.8. Copper sulphate (100 g) and 4-Aminoantipyrine (2 g) was separately dissolved in 100 mL of distilled water. From 5% H_3PO_4 10 mL were diluted to 100mL in a volumetric flask. Potassium ferricyanide (2 g) was dissolved in 25ml of distilled water and stored in a brown bottle.

Phenol (1 g) was dissolved in 1000ml of freshly boiled, cooled distilled water and standardized. For standardization 50ml of stock phenol solution was added to100ml distilled water followed by 10ml of 0.1 N bromate-bromide solution and 1ml of concentrated HCl with gentle swirl.10 mL portions of bromate-bromide solution was added if brown colour of free bromine gives up then after 10 minutes KI (1g) was added swirled gently and kept for some time. A blank was prepared in the same manner using distilled water and 10ml 0.1 N bromate-bromide solution. Blank and sample were titrated with 0.025 N sodium thiosulphate using starch as an indicator. Concentration of phenol was calculated as:

Mg/L Phenol= 7.842 [CA ^{x} B - C] (1)

Where A, C stands for sodium thiosulphate (ml) used for blank and stock phenol solution respectively, and B for bromate-bromide solution (ml) used for stock phenol solution divided by 10.

2.3 Batch adsorption procedure

Standardize solution of phenol was employed after dilution for batch biosorption studies by using powder biomass of Parthenium hysterophorus. Sorption protocol was designed to investigate the effect of contact time and biomass dosage (0.01–0.06 g) on phenol remediation. Sorbate with fixed initial concentration was contacted with sorbent in separate flasks till attainment of equilibrium at room temperature. Contact of sorbate and sorbent was terminated by filtration according to predetermined time intervals. After filtration 0.5 mL of ammonium hydroxide, 0.2 mL of 4- Aminoantipyrene and 0.2 mL of Potassium ferricyanide solutions were added to 20ml of sorbate and blank by adjusting pH to 7.9 with phosphate buffer by using pH meter (inolab-720). Blank was used as reference for determining absorbance of phenol standard solution by UV/Vis spectrophotometer (PerkinElmer's LAMBDA 25). Phenol uptake by biomass was calculated as percentage (%R) using the equation:

$$\%R = \left(\frac{C_i - C_t}{C_i}\right) 100 \quad (2)$$

The biosorption efficiency q_e (mg/g) was calculated using:

$$q_e = \left(\frac{C_i - C_e}{W}\right) V \quad (3)$$

where C_i, C_t and C_e (mg/L) are the liquid phase concentration of phenol initially, at time t and at equilibrium, respectively. V is the volume (L) of the solution and W is weight (g/L) of sorbent.

3. Results and discussion

3.1 Characterization of sorbent

3.1.1 FTIR analysis

Biomass in native and sorbed form was analysed using FTIR (Thermo Scientific USA NICOLET-6700) spectroscopy to figure out qualitatively basic functional groups on surface. FTIR spectrum of native PH reveals a less intense peak in the range 2915-2935cm^{-1} (**Figure 1**) corresponded to aliphatic C-H asymmetric stretching vibrations of meth-

ylene hydrogen's[12]. A peak at 2345–2364 cm^{-1} corresponded to P–H vibrations from phosphorus[13]. A sharp intense peak at 1739cm^{-1} corresponded to (C=O) stretching vibrations of aldehydes/ester[14] while peak at 1370cm^{-1} was attributed to weak C-O stretching vibrations in cellulose[15]. Prominent peaks between 1300 and 1000 cm^{-1} were due to the presence of phenolic and alcoholic moiety[16].

Appearance of strong broad band at 3600–3200 cm^{-1} corresponded to H-bonded OH groups of phenols[17] suggests phenol sorption from synthetic solution onto biomass surface. A band from 2923–2800 cm^{-1} on phenol adsorbed PH can be ascribed to aldehydes C-H group. Absorbance peak between 1600–1675 cm^{-1} could be attributed to C = C stretching vibrations of alkenes[16]. A band from 990–1050 cm^{-1} with a peak at 1016 cm^{-1} represented (P-O-C) stretching vibrations of aliphatic phosphates[12].

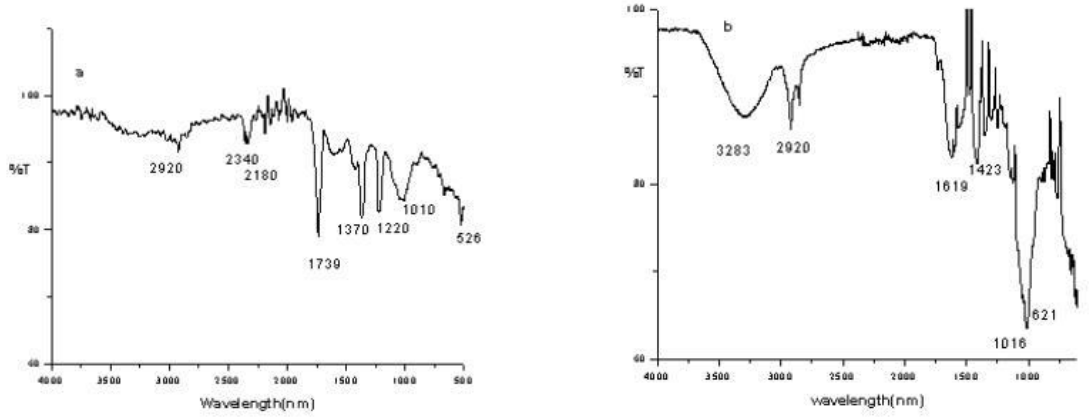

Figure 1. FTIR spectrum (a) of native and (b) phenol sorbed biomass

3.1.2 SEM analysis

The SEM images (**Figure 2A**) represent rough texture and heterogeneous distribution of pores on the surface of biomass. The pore openings apparent at 4000X magnification could offer accessibility of pollutant into internal pores[18] vital for the adsorption purposes[19]. Indication about biomass high surface area is reflected by **Figure 2B**, sort of swelling or scaling is apparent on biomass surface after loading of phenol.

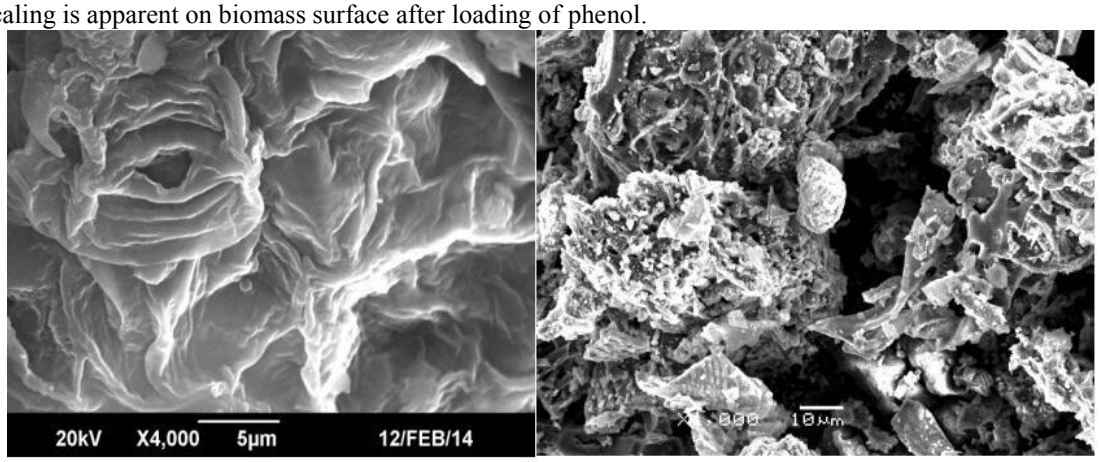

Figure 2. SEM images of native (**a**) and phenol sorbed (**b**) biomass

3.2 Time/dose optimization for adsorption

Concentration of phenol stock solution calculated by equation (1) comes out to be 17.432 mg/L; working standard of 4.5 mg/L concentration was prepared from it and contacted with 0.03 g of biomass in separate flasks to determine the influence of contact time. Absorbance of filtrate against blank was measured at 500 nm, revealing regular uptake of phenol establishing equilibrium attainment within 120 minutes (**Figure 3**)

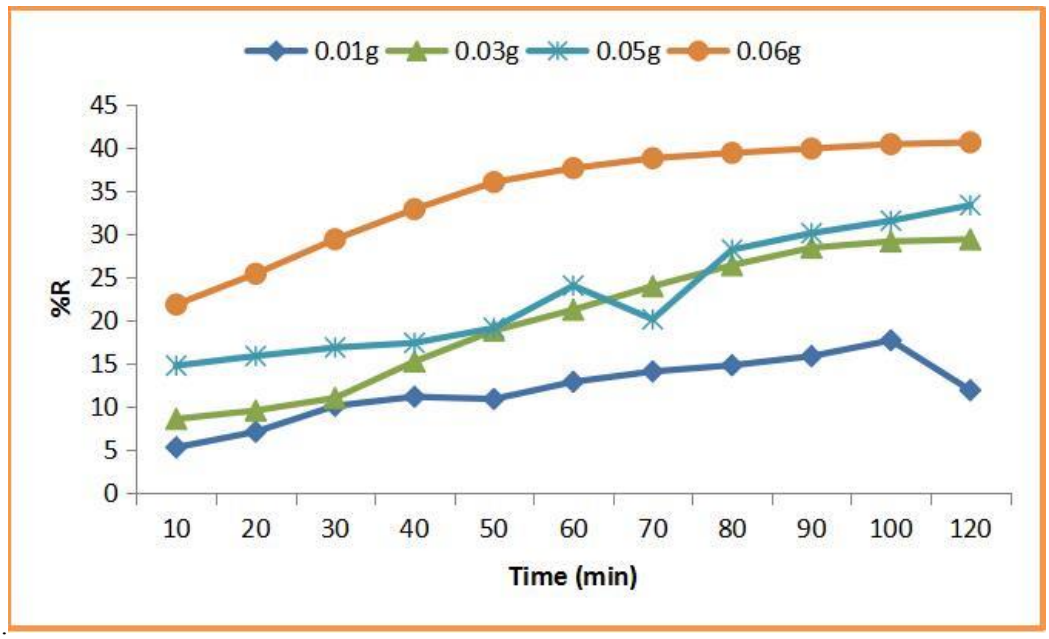

Figure 3. Effect of adsorbent dose on removal efficiency for phenol

The effect of dosage at values higher and lower than 0.03 g indicates that the removal efficiency generally increased as the dose concentration increased. Probably highest dose provided increased surface area or alternatively more sorption sites[20].

Similarly Zaid *et al*., (2008) reported K_d values increase with increasing dose, and removal enhancement from 25% to 90% by increasing adsorbent dose on the adsorption of MB dye[21].

3.3 Sorption kinetic study

To facilitate the mechanism of sorption reactions and to get valuable insight into the reaction pathways the study of kinetics in wastewater treatment is important. Therefore transport mechanism of phenol from aqueous media onto solid support is figured out through reaction and diffusion based models. The calculated and experimental values of sorption capacity (q_e), rate constants (k), and correlation coefficients (R^2) values are listed in **Table 1**.

3.3.1 Pseudo-first order

The linear form of Lagergren pseudo-first order kinetic model is:

$$\log(q_e - q_t) = \log q_e - \left(\frac{k_1}{2.303}\right)t \qquad (4)$$

Rate constant (k_1) and equilibrium amount of pollutant (q_e) can be obtained from slope and intercept of plot between log ($q_e - q_t$) against time (t).

	Pseudo first-order				Pseudo second-order			
m (g)	q_e(exp) (mg/g)	q_e(cal) (mg/g)	K_1 (min^{-1})	R^2	q_e(cal) (mg/g)	h (mg/g min)	k_2 ($gmg^{-1}min^{-1}$)	R^2
0.01	2.10	1.00	0.21	0.11	0.87	33.67	25.28	0.76
0.02	1.66	1.00	0.19	0.84	0.78	98.68	60.28	0.61
0.03	1.74	1.00	0.42	0.91	1.29	93.90	155.59	0.85
0.05	1.82	1.00	0.23	0.93	2.02	97.50	397.07	0.82
0.06	1.65	1.00	0.15	0.84	2.35	33.81	186.05	1.00

Table 1. Reaction based kinetics for phenol adsorption against adsorbent dosage

3.3.2 Pseudo-second order

Sorption capacity of the solid phase identification by linear form of pseudo-second order is:

$$\frac{t}{q_t} = \frac{1}{k_2 q_e^2} + \left(\frac{1}{q_e}\right)t \qquad (5)$$

Initial sorption rate, h (mg/g min), at t→0 can be defined as:

$$h = k_2 q_e^2 \qquad (6)$$

Linear plot of t/q_t against t result in a straight line, q_e and h values can be obtained from slope and intercept of plot (**Figure 4**). A decrease in the initial rate of adsorption was observed by increasing adsorbent amount, possibly due to the

decrease in driving force (see **Table 1**). It is clear from values of h, that 0.02g is optimum mass at which maximum adsorption of phenol took place. Calculated biosorption capacity by pseudo-first order rate equation is found lower in comparison to experimental values. The correlation coefficients for both kinetic models is noted quite irregular and low, suggesting them as not rate limiting. Secondly the deduction of best fit for these models is inadequate owing to variations between actual and estimated values of q_e. Similarly less significance of pseudo first order kinetic model is reported for phenol sorption by activated carbon[22] and activated phosphate rock[23]. Whereas opposit to current study is favorability of pseudo second order model reported by elsewhere[24].

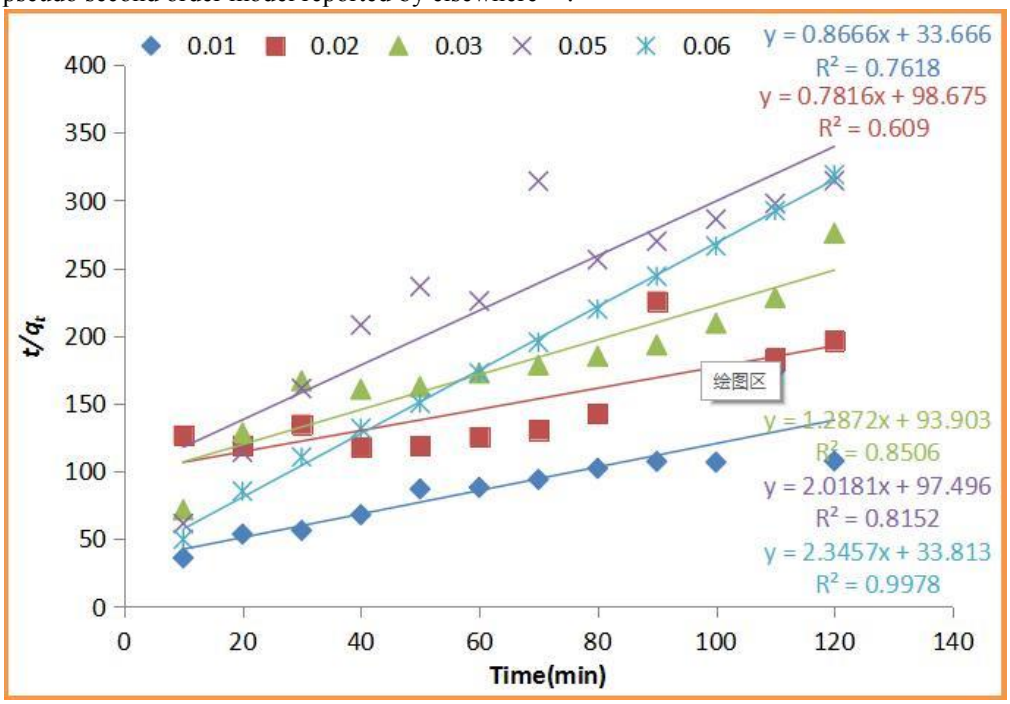

Figure 4. Pseudo second order kinetic plot for phenol sorption

3.3.3 Intraparticle diffusion model

The mechanism of diffusion was not identified by the kinetic models thus on the basis of theory projected by Weber and Morris (1962)[25], intrraparticle diffusion model (IPD) was used. It is an empirically found functional relationship which shows that variation of uptake is proportional to $t^{1/2}$ to a certain extent than with the contact time t. Equation can be represented as:

$$q_t = k_{id} t^{1/2} + C \qquad (7)$$

Where k_{id} is rate constant of intrraparticle (pore) diffusion (mg/g $min^{0.5}$) and C is boundary layer thickness. Straight line is obtained (**Figure 5**) by plotting graph between q_t and $t^{1/2}$. The values of k_{id} indicate that the intrraparticle diffusion becomes more prominent with an increase in adsorbent amount (see **Table 2**). Similarly values of intercept C also increase and by expansion, it indicates that boundary layer effect increases at alleviating dosage.

3.3.4 The Elovich model

The linear form of Elovich equation is:

$$q_t = \frac{1}{\beta}\ln(\alpha\beta) + \frac{1}{\beta}\ln t \qquad (8)$$

Where q_t is the amount adsorbed (mg/g) at time t, α is the initial sorption rate, (mg/g min), and β is the desorption constant (g/mg). Plot of q_t versus lnt give straight line and the values of α and β were calculated from slope and intercept of straight line. It can be figured out (**Table 2**) from values of α that adsorption rate decreases by increasing adsorbent amount, simultaneously desorption of sorbed phenol molecules from PH surface is indicated by increasing trend of β values

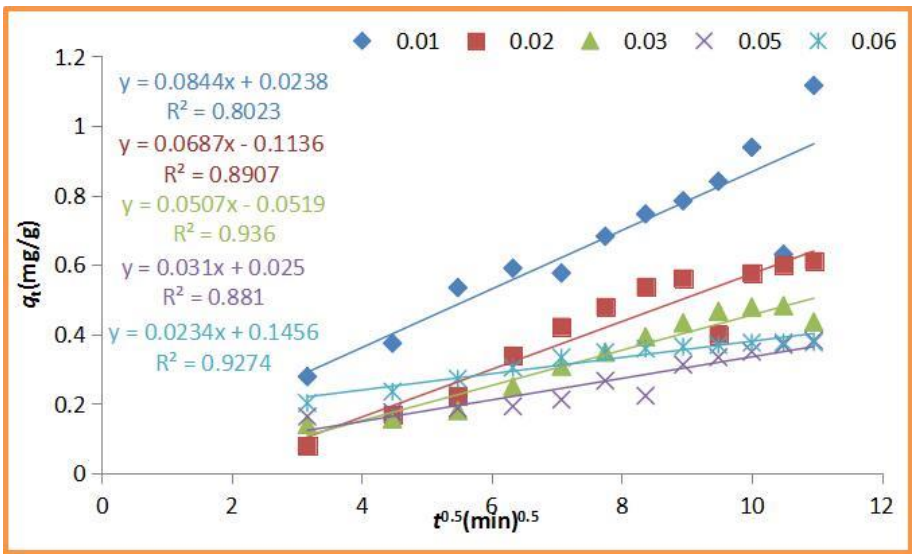

Figure 5. Intraparticle diffusion model for the sorption of phenol

Correlation coefficient values signify supremacy of IPD model to Elovich, which reveals that the molecular diffusion of phenol molecules on the surface of adsorbent played a major function in its removal. Similarly IPD significance for phenol adsorption is reported by Ruey *et al*., (2000) on activated carbon Prepared from Plum Kernels and Abdelwahab *et al*., (2013) on Luffa cylindrica fiber[26,27].

	Intra particle diffusion			**Elovich**		
m (g)	k_{ip} (mg/g/min$^{0.5}$)	**C**	**R^2**	**α (mg/g/min)**	**β (g/mg)**	**R^2**
0.01	0.08	0.02	0.80	0.36	3.34	0.46
0.02	0.07	-0.11	0.89	0.27	3.59	0.66
0.03	0.05	-0.05	0.94	0.21	4.81	0.71
0.05	0.03	0.03	0.88	0.12	8.68	0.55
0.06	0.02	0.15	0.93	0.11	10.91	0.64

Table 2. Estimated rate constants for phenol adsorption by diffusion based model

3.4 Sorption isotherms study

Adsorption isotherms are used to describe the interaction of solute particles with adsorbents, and are significant for optimizing the use of adsorbents[28]. Most frequently experienced isotherms are Langmuir and Freundlich. Recent study explores Temkin, Dubinin-Radushkevich and Flory-Huggins isotherms including most tested one for sorption of phenol by variable doses of adsorbent.

3.4.1 The Langmuir isotherm

Langmuir model assumes monolayer adsorption of material in liquid over a homogenous surface of adsorbent at a constant temperature; its equation in linear form is:

$$\frac{C_e}{q_e} = \frac{1}{q_m K_L} + \frac{C_e}{q_m} \qquad (9)$$

where q_m is the maximum adsorption capacity (mg/g) and K_L is a constant associated to the binding sites affinity (L/mg). A graph of C_e/q_e versus C_e yields a straight line with a slope and intercept from which q_m and k_L can be calculated. Value of q_m was found contradictory to the experimentally determined biosorption capacity, secondly value of R^2 (0.28) shows that Langmuir model is not followed for adsorption of phenol by PH.

3.4.2 Freundlich Isotherm

Freundlich isotherm model reported in literature[29,30], assumes that the process of adsorption takes place on a non-uniform surface. The linear form of equation is:

$$log q_e = log K_F + \log C_e^{1/n} \qquad (10)$$

Where K_F ((L/mg) is used to express the adsorption capacity and 1/n is the strength of adsorption, it indicates both the heterogeneity of the adsorbent sites as well as relative distribution of energy. Nature of sorption identified from value of 1/n (0.29) indicates its favourability, as type of isotherm will be irreversible if (1/n = 0), favourable (0 < 1/n < 1),

and unfavourable (1/n > 1) (Theivarasu and Mylsamy, 2011). Still R^2 does not support Freundlich model as best fit.

3.4.3 Temkin Isotherm

This model assumes that the adsorption process is indirectly affected by the adsorbate/adsorbent interactions (Da-da, 2012). Expressed in linear form as:

$$q_e = \frac{RT}{b_T} ln K_T + \frac{RT}{b_T} ln C_e \quad (11)$$

where R is general gas constant (0.008314 kJ/mol K), T is absolute temperature (K), $1/b_T$ is sorption heat constant (KJ/mol), and K_T (L/g) is adsorption capacity referred as adsorption

Isotherms	parameters	Values	Isotherms	Parameters	Values
Langmuir	q_m (mg/g)	-0.28	Dubbin-Radushkevich	K_{DR}	10.97
	K_L(L/mg)	-0.36		q_m	4.81
	R^2	0.31		R^2	0.53
Freundlich	N	0.29		E	0.21
	K_F(mg/g)	0.72	Flory Huggins	α_{FH}	-2.87
	R^2	0.57		K_{FH}	0.06
Temkin	B	0.98		R^2	0.90
	K_T	-2.87		ΔG °	-7.09
	R^2	0.67			

Table 3. Isotherms model constants and their respective coefficients for phenol sorption constant. Values of $1/b_T$ and K_T can be calculated from slope and intercept of a plot between q_e and lnC_e. Heat of sorption identified by this model indicates weak sorbent sorbate interaction.

3.4.4 The Dubinin-Radushkevich isotherm

This isotherm is reported by Radushkevich (1949) and Dubinin (1965) describing a relation between sorption curve and the porous structure of the sorbent[31]. It is generally represented by equation:

$$\ln q_e = \ln q_m - K_{DR}\varepsilon^2 \quad (12)$$

where K_{DR} is a constant and is associated with the mean free energy of sorption per mole of the sorbate. This energy can be calculated by equation,

$$E = \frac{1}{\sqrt{2K_{DR}}} \quad (13)$$

The calculated value of E is 0.21 KJ/mol less than 8 KJ/mol[32], indicates physiosorption of phenol on PH surface. The calculated maximum biosorption capacity was noted very high than experimental value in addition to low value of correlation coefficient.

3.4.5 Flory Huggins isotherm

The degree of surface coverage of adsorbate on adsorbent can be expressed in linear form according to Flory – Huggins model as:

$$\log\left(\frac{\theta}{C_e}\right) = \log K_{FH} + \alpha_{FH}\log(1-\theta) \quad (14)$$

where θ is the degree of surface coverage, can be computed by:

$$\theta = \frac{1-C_e}{C_i} \quad (15)$$

α_{FH} is the number of metal ions occupying sorption sites and K_{FH} the equilibrium constant of adsorption[33]. The values of K_{FH} and α_{FH} can be obtained from intercept and slope of the plot of log (θ/C_e) versus log (1- θ) respectively. Moreover the equilibrium constant K_{FH} can be used to compute the Gibbs free energy for sorption process. The Gibbs free energy is related to equilibrium constant as follow:

$$\Delta G^{\circ} = -RT\ln K_{FH} \quad (16)$$

A positive correlation is inferred from data of surface coverage (θ) with increase in sorbent concentration, the effect is found increasing from 21% to 41% by increasing biomass dosage from 0.01g to 0.06g. The negative value of ΔG° shows feasibility and spontaneous nature of the process. Fitness approximation calculates phenol sorption onto PH by this model due to highest R^2 value (see **Table 2**).

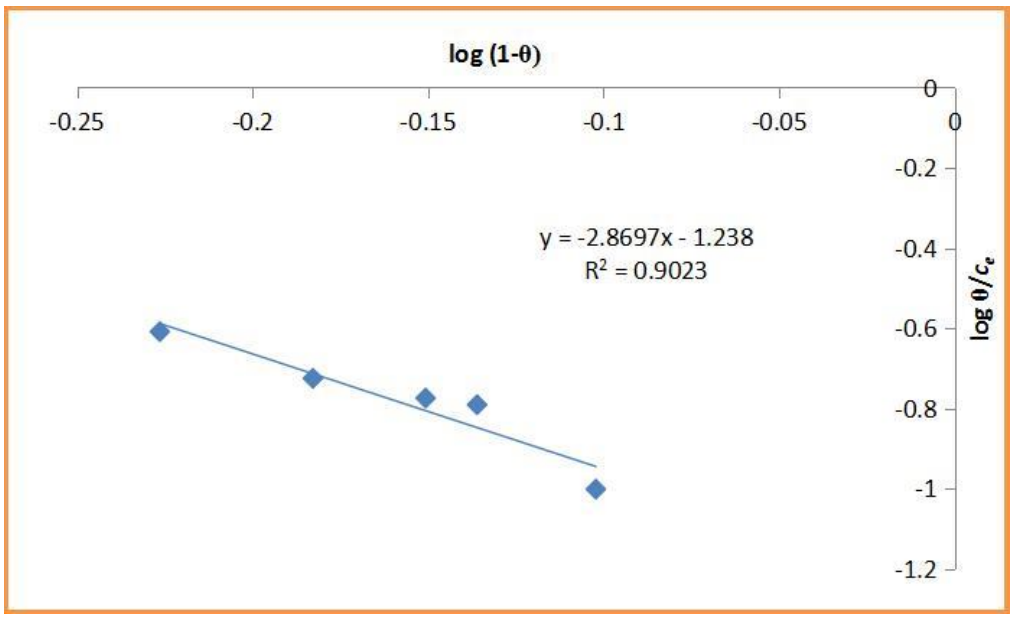

Figure 6. Flory Huggins model for adsorption of phenols

Similarly Flory Huggins isotherm was appreciably followed for the adsorption of Cu(ii) on coconut (Cocos nucifera L.) coir dust and for adsorption of lead (ii) ions from aqueous solution using coir dust (cocos nucifera l.) And it's modified extract resins[34]. On the contrary Langmuir and Freundlich isotherm models were followed for the adsorption of phenol on granular activated carbon from nutrient medium[35], and Cr-bentonite[36].

Acknowledgements

National Centre for Physics (NCP) is greatly acknowledged for generously guiding and sparing resources for the work to complete. Similarly, HEC Pakistan is highly thanked for financing the research project.

Conclusions

The positive correlation was noted for adsorption of phenol enhancement with an increase of biomass dosage. The Intraparticle diffusion of phenol onto adsorbent surface was identified to be the rate limiting step. Flory-Huggins gave a better fit to all adsorption isotherms than the Langmuir, Freundlich, Temkin, and Dubinin-Radushkevich, and the remediation process was figured out as a physical adsorption rather than a chemical one.

References

1. Wake H. Oil refineries: A review of their ecological impacts on the aquatic environment. Estuarine, Coastal and Shelf Science, 2005, 62(1–2): 131–140.
2. Kujawski W, Warzawski A, Ratajczak W, *et al*. Application of pervaporation and adsorption to the phenol removal from wastewater. Separation & Purification Technology, 2004, 40(2): 123–132.
3. Srivastava VC, Swamy MM, Mall ID, *et al*. Adsorptive removal of phenol by bagasse fly ash and activated carbon. Colloids & Surfaces A Physicochemical & Engineerimg Aspects, 2006, 272(1): 89–104.
4. Olafadehan OA, Aribike DS. Treatment of industrial wastewater effluent. Journal of Nigerian Society of Chemical Engineers, 2000, 19: 50–53.
5. Radhika M, Palanivelu K. Adsorptive removal of chlorophenols from aqueous solution by low cost adsorbent-Kinetics and isotherm analysis. Journal of Hazardous Materials, 2006, 138(1): 116–124.
6. Hameed BH, Rahman AA. Removal of phenol from aqueous solutions by adsorption onto activated carbon prepared from biomass material. Journal of Hazardous Materials, 2008, 160(2): 576–581.
7. Aygun A, Karakas YS, Duman I. Production of granular activated carbon from fruit stones and nutshells and evalua tion of their physical, chemical and adsorption properties. Microporous & Mesoporous Materials, 2003, 66(2): 189–195.
8. Karunarathnea HDSS, Amarasinghea BMWPK. Fixed bed adsorption column studies for the removal of aqueous phenol from activated carbon prepared from sugarcane bagasse. Energy Procedia, 2013, 34(40): 83–90.
9. Taha S, Cisse S, Dorange IG. Heavy metals removal by adsorption onto peanut husks carbon: Characterization kinet ic study and modeling. Separation & Purification Technology, 2001, 24(3): 389–401.
10. Namasivayam C, Kavitha D. IR, XRD and SEM studies on the mechanism of adsorption of dyes and phenols by coir pith carbon from aqueous phase. Microchemical Journal, 2006, 82(1): 43–48.
11. Shiundu PM, Mbui DN, Ndonye RM, *et al*. Adsorption and detection of some phenolic compounds by rice husk ash of Kenyan origin. Journal of Environmental Monitoring Jem, 2002, 4(6): 978–984.

12. Daizy R, Harminder B, Singh P, *et al*. Phytotoxic effect of Parthenium residues on the selected soil properties and growth of chickpea and radish. Weed Biology and Management, 2002, 2(2): 73–78.
13. Louhi A, Hammadi A, Achouri A. Determination of some heavy metal pollutants in sediments of the Seybouse river in Annaba, Algeria. Air, Soil and Water Research, 2012, 5(5): 91–101.
14. Elumalai S, Sakthivel R. GC-MS and FT-IR spectroscopic determination of Fattyacid Methyl Ester of 16 freshwater Microalgae, isolated from cement industries of Tamil Nadu, India. J. Algal Biomass Utln, 2013, 4(1): 50–69.
15. Yu P, Block H, Niu Z. Rapid characterization of molecular chemistry, nutrient make-up and microlocation of internal seed tissue. Journal of Synchrotron Radiation, 2007, 14(4): 382–390.
16. Wetzel DL, Eilert AJ, Pietrzak LN, *et al*. Ultraspatially-resolved synchrotron infrared microspectroscopy of plant tissue. Cell Mol Biol (Noisy-le-grand), 1998, 44(1): 145–167.
17. Abdullah N, Suleiman F, Gerhauser H. Characterisation of oil palm empty fruit bunches for fuel application. Journal of Physical Science, 2011, 22(1): 1–24.
18. Amir S, Hafidi M, Merlina G, *et al*. Elemental analysis, FTIR and 13C-NMR of humic acids from sewage sludge composting. Agronomie, 2004, 24(1): 13–18.
19. Sugumaran P, Susan PV, Ravichandran P, *et al*. Production and characterization of activated carbon from banana empty fruit bunch and Delonix regia fruit pod. Journal of Sustainable Energy and Environment, 2012, 3: 125–132.
20. Stavropoulos GG, Samaras P, Sakellaropoulos GP. Effect of activated carbons modification on porosity, surface structure and phenol adsorption. Journal of Hazardous Materials, 2008, 151(2–3): 414–421.
21. Boudrahem F, Aissani-Benissad F, Soualah A. Kinetic and equilibrium study of the sorption of Lead(II) Ions from aqueous phase by activated carbon. Arabian Journal for Science & Engineering, 2013, 38(8): 1939–1949.
22. Al-Anber ZA, Al-Anber M. Thermodynamics and kinetic studies of Iron(III) adsorption by olive cake in a batch system. Journal of the Mexican Chemical Society, 2008, 52(2): 108–115.
23. Awala HA, El Jamal MM. Equilibrium and kinetics study of adsorption of some dyes onto Feldspar. Journal of the University of Chemical Technology and Metallurgy, 2011, 46: 45–52.
24. Alzaydien SA, Manasreh W. Equilibrium, kinetic and thermodynamic studies on the adsorption of phenol onto activated phosphate rock. International Journal of Physical Sciences, 2009, 4(4): 172–181.
25. Muthamilsevi P, Poonguzhali E, Karthikeyan R. Removal of phenol from aquous solution by adsorption. International journal of advanced research in engineering and technology IJARET, 2012, 3: 280–288.
26. Sutherland C, Venkobachar C. A diffusion-chemisorption kinetic model for simulating biosorption using forest macro-fungus, Fomes fasciatus, International Research Journal of Plant Science, 2010, 1: 107–117.
27. Juang R, Wu F, Tseng R. Mechanism of adsorption of dyes and phenols from water using activated carbons prepared from Plum Kernels. Journal of Colloid and Interface Science, 2000, 227: 437–444.
28. Kumar D, Subbaiah VM, Reddy AS, *et al*. Biosorption of phenolic compounds from aqueous solutions onto Chitosan-Aabrus Precatorius blended beads. J Chem Technol Biotechnol, 2009, 84: 972–981.
29. Annadurai G, Juang SR, Lee DJ. Use of Cellulose-based wastes for adsorption of dyes from aqueous solutions. Journal of Hazardous Materials. 92, (2002)263-274.
30. Zhao X, Urano K, Ogasawara S. Adsorption of Polyethylene Glycol from Aqueous Solution on MontRillonite Clays. Colloid and Polymer Science, 1989, 267: 899–906.
31. Theivarasu C, Mylsamy S. Removal of malachite green from aqueous solution by activated carbon developed from Cocoa (Theobroma Cacao) Shell-A Kinetic and Equilibrium Studies. E-Journal of Chemistry, 2011, 8: 363–371.
32. Dada AO, Olalekan AP, Olatunya AM, *et al*. Freundlich, Temkin and Dubinin–Radushkevich isotherms studies of equilibrium sorption of Zn^{2+} unto Phosphoric Acid modified rice husk. IOSR Journal of Applied Chemistry, 20112, 3: 38–45.
33. Aikpokpodion PE, Osobamiro T, Atewolara-Odule OC, *et al*. Studies on adsorption mechanism and kinetics of magnesium in selected cocoa growing soils in Nigeria. Journal of Chemical and Pharmaceutical Research, 2013, 5: 128–1399.
34. Israel AA, Okon O, Umoren S, *et al*. Kinetic and equilibrium studies of adsorption of lead (ii) ions from aqueous solution using coir dust (cocos nucifera l.) And it's modified extract resins. The Holistic Approach to Environment, 2013, 34: 209–222.
35. Dabhade MA, Saidutta MB, Murthy DVR, Adsorption of phenol on granular activated carbon from nutrient medium: Equilibrium and kinetic study. International Journal of Environmental Research, 2009, 3: 557–568.
36. Zheng H, Wang Y, Zheng Y, *et al*. Equilibrium, kinetic and thermodynamic studies on the sorption of 4-hydroxyphenol on Cr-bentonite. Chemical Engineering Journal, 2008, 143: 117–123.

Applied Chemical Engineering (2019) Volume 2 Issue 2
doi:10.24294/ace.v1i2.624

Adsorption of Toxic Indigo Carmen Dyestuff from Aqueous Solution by Chitosan and Chitosan Phthalate

Selma Ekinci, Fuat Guzel

Department of Chemistry, Batman University, Batman, Turkey

ABSTRACT

Toxic indigo carmen dyestuff was removed from the aqueous solution by adsorption. Adsorption was examined kinetically and thermodynamically based on temperature. Derivative of chitosan which is called chitosan phthalate was synthesized and used in removal of indigo carmen from aqueous solution. Some kinetic and thermodynamic parameters were calculated. Adsorption isotherms were drawn. Lastly, the adsorption of indigo carmen from the aqueous solution by chitosan and chitosan phthalate were compared.

Keywords: Adsorption; Indigo carmen; Dyestuff; Chitosan

1. Introduction

Dyestuffs are organic compounds that are used to color objects. Synthetic dyestuffs have a complex aromatic structure containing units such as benzene, toluene, xylene and anthracene. This complex aromatic structure allows the dyestuffs to be highly stable and resistant to biochemical degradation[1]. The use of synthetic dyes in textile, leather, rubber, food, paper, plastic, pharmaceutical and cosmetic industries is increasing day by day. Dyestuffs which are left in water after being used in industrial processes leave some deleterious effects on human and aquatic life. Many of these harmful dyestuffs are toxic and carcinogenic[2]. Many physical, chemical and biological decolorization methods have been developed to remove dyestuffs that are highly resistant to heat, light and oxidizing agents from waste water. These are chemical precipitation, reverse osmosis, membrane filtration, ozonation, oxidation, ion exchange, irradiation and adsorption. Among these methods, the process which gives the best result is the adsorption technique. Besides, it is known as a low-cost technique[3-6].

Chitosan is a deactylated derivative of chitin. It is the most commonly found polysaccharide in nature after cellulose. Chitosan can be obtained from the shell of shrimps, mushrooms, crabs and insects[7]. Chitosan which is a natural biosorbent, is a good adsorbent for removing harmful dyestuffs in industrial wastewater. It is non-toxic and low cost[8]. As it contains both amino and hydroxyl groups, chitosan can easily be modified[9,10]. This study analyzes kinetic and thermodynamic properties of the adsorption of toxic indigo carmen (IC) dyestuff from aqueous solution by chitosan and its synthesized derivative chitosan phthalate.

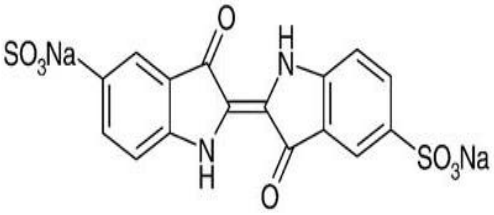

(a)

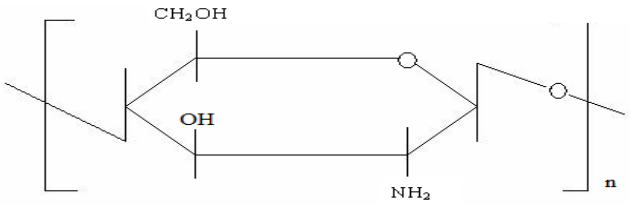

(b)

Figure 1. Molecular structure of chitosan and indigo carmine

2. Experimental Studies

2.1 Adsorption Kinetics

Adsorbate- adsorbent equilibrium contact time is found by understanding adsorption kinetics. For determining this

doi: 10.24294/ace.v1i2.624

contact time, 0,1 gram of chitosan/chitosan phthalate were added to 50 ml of indigo carmine (IC) solutions whose initial concentrations are 200 ppm. This mixture was shaken for 12 hours at 293 K. During this time, samples were taken from each solution at different time intervals and absorbance values were determined with UV- spectrophotometer. This process was repeated at 313 and 333 K.

The data obtained from kinetical experiments were applied to the following equations: The Lagergren (equ.1)[11], the Arrhenius (equ.2)[12] and the intrapartical diffusion (Equ. 3,4)[13] rate equations.

$$\log(q_e - q) = \log q_e - \frac{k_{ads,1}}{,303}.t \quad (1)$$

$$\log k_{ads,1} = \log Z_e \quad \frac{E_a}{2,303RT} x \frac{}{T} \quad (2)$$

$$q = k_p . t^{1/2} \quad (3)$$

$$\frac{t}{q} = \frac{1}{k_{ads,2}\, q_e^2} + \frac{t}{q_e} \quad (4)$$

2.2 Preparation of Chitosan Phthalate

1 g chitosan (6,2 mmol) was dissolved in the acetic acid solution (% 1, 100 ml). Then, a solution of the phthalic anhydride (6.25 mmol) in pyridine (5 mL) was added dropwise to the mixture with vigorous stirring. pH of reaction was calibrated at 7.0 by the dropwise addition of NaOH solution (1.0 M). After 40 minutes, the reaction was terminated by the addition of NaCl aqueous solution (%20, 200 mL). The resulting precipitate was filtered, washed with acetone and diethyl ether, and desiccated to give chitosan phthalate conjugates[14].

2.3 Adsorption Thermodynamics

After kinetical study, the equilibrium contact time of adsorption was determined. Then 50 ml of IC solutions at different initial concentrations were prepared and 0,1 g of chitosan/chitosan phthalate was added to each solutions. This mixture was shaken during the equilibrium contact time at 293, 313 and 333 K. After shaking, absorbance values of solutions remaining from adsorption (C_e) were measured and the amount of IC which is adsorbed (q_e) was calculated. Then, the adsorption isotherms were drawn. Adsorption isotherm of chitosan and IC was suitable with Langmuir İsotherm. The adsorption isotherm of chitosan phthalate and IC was suitable with H-type isotherm according to isotherm classification made by Giles. Langmuir constants C_m (connected with adsorption capacity) and b (connected with adsorption energy) were calculated for the adsorption of chitosan and IC. b constants values were applied to the following equations:

$$\log b = \log A \quad \frac{\Delta H}{2,303R} \frac{1}{T} \quad (5)$$

$$\Delta G = -RT \ln b \quad (6)$$

$$\Delta G = \Delta H - T.\Delta S \quad (7)$$

3. Results

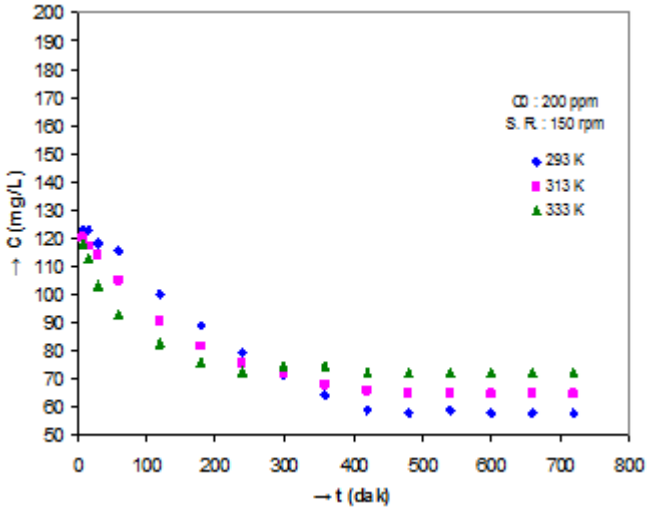

Figure 2. The effect of contact time on the adsorption of chitosan and IC.

According to **Figure 2**, chitosan adsorbed more IC at 293 K. and, as the equilibrium contact time of adsorption is shorter, we can say that IC was adsorbed faster at 333 K. by chitosan. Therefore, a chemical adsorption occurs between chitosan and IC at high temperatures.

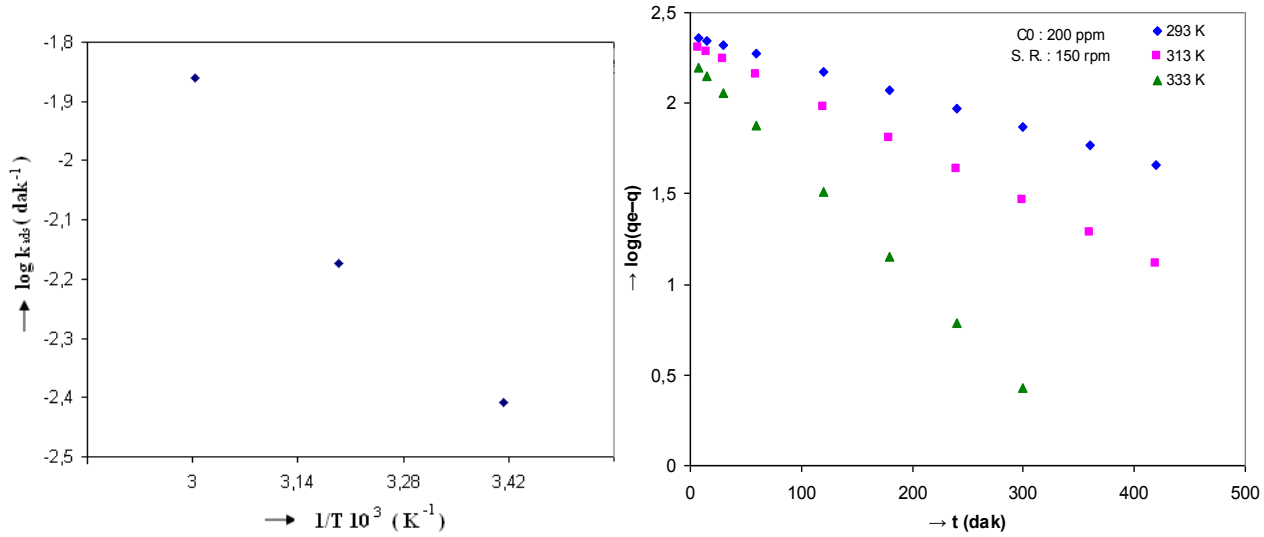

(a)

(b)

Figure 3. Lagergren (a) and Arrhenius (b) drawings of adsorption of chitosan and IC.

Adsorption rate constants k_{ads} were calculated from Lagergren drawings. q_e (mmol/L); is the amount of adsorbate adsorbed at equilibrium time and q (mmol/L); is the amount of adsorbate adsorbed at any time. k_{ads} values were determined as 0,0037; 0,0063 and 0,0135 (min^{-1}) at 293, 313 and 333 K respectively. This k_{ads} values were evaluated at Arrhenius equation and activation energy of adsorption was calculated as 25, 628 kJ/mol. k_{ads} values also show chitosan adsorbed more IC at high temperature.

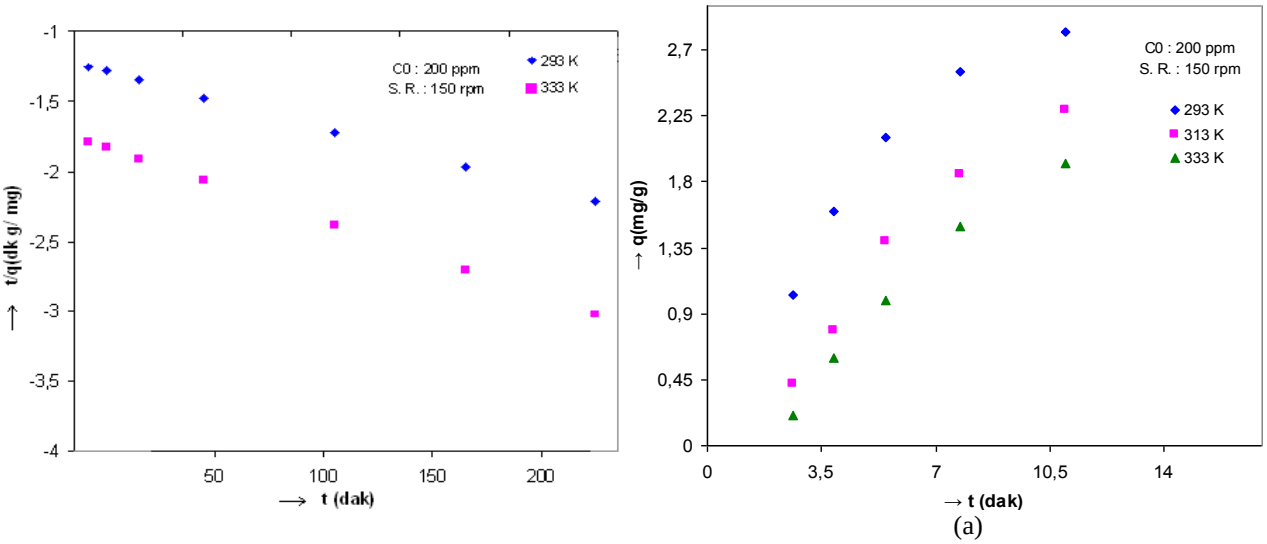

(a)

(b)

Figure 4. Weber-Morris (a) and Ho-Mckay (b) drawings of adsorption of chitosan and IC.

The data obtained from experiments were also applied to the Weber- Morris and Ho-Mckay equations and intra-

particle rate constants (k_p) were calculated. k_p values are 3,93; 4,02; 4,54 ($min^{-1/2}$) at 293, 313 and 333 K respectively.

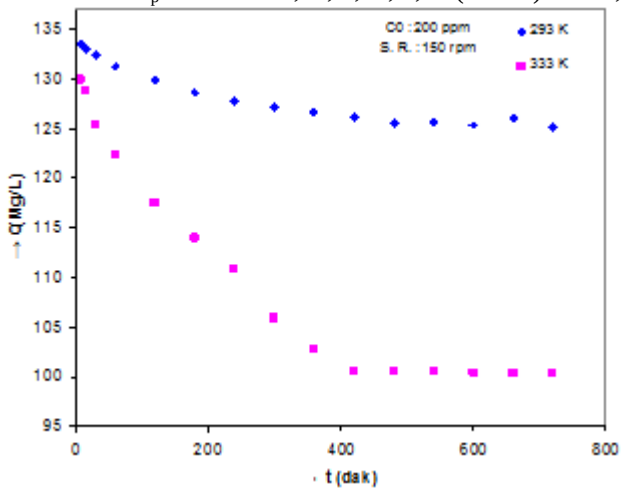

Figure 5. The effect of contact time on the adsorption of chitosan phthalate and IC.

Figure 5 shows that chitosan phthalate adsorbed more IC at 333 K. Chitosan phthalate has amino groups and IC has $–SO_3$ groups. Amino groups have a positive charge in the IC solution. There is strong chemical adsorption between these amino groups and $–SO_3$ groups. So, we can say that the adsorption between chitosan phthalate and IC is chemical adsorption. For this reason, chitosan phthalate adsorbed more IC at higher temperature.

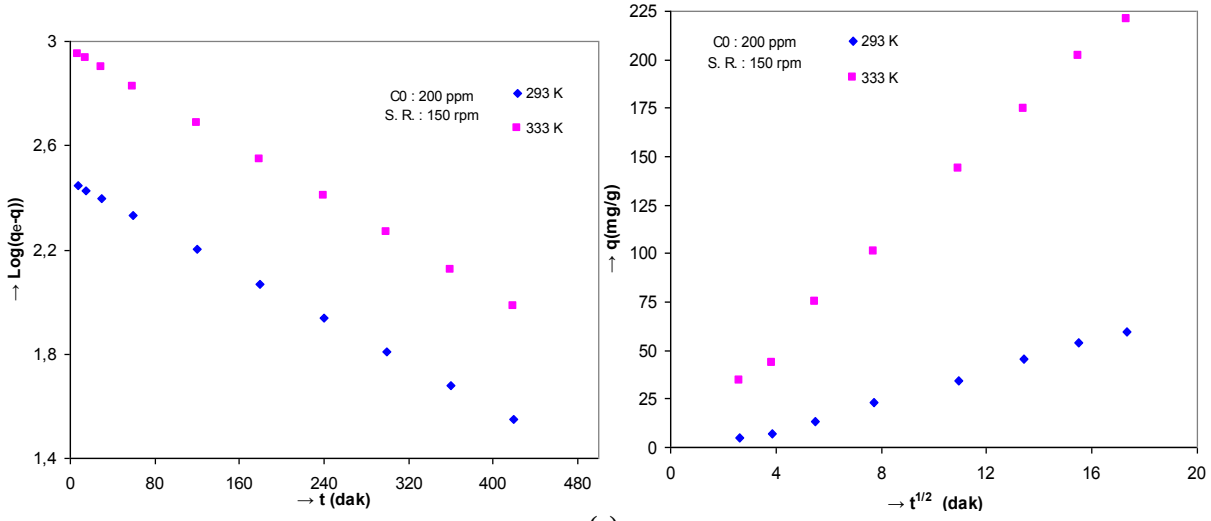

(a)
(b)

Figure 6. Lagergren (a) and Weber- Morris (b) drawings of adsorption of chitosan phthalate and IC.

Adsorption rate constants k_{ads} were calculated from Lagergren drawings and intraparticle diffusion rate constants were calculated according to Weber- Morris drawings. k_{ads} values are 0, 0049 and 0, 0053 min^{-1} at 293 and 333 K respectively. k_p values are 3, 9824 and 13, 1233 $min^{-1/2}$ at 293 and 333 K respectively.

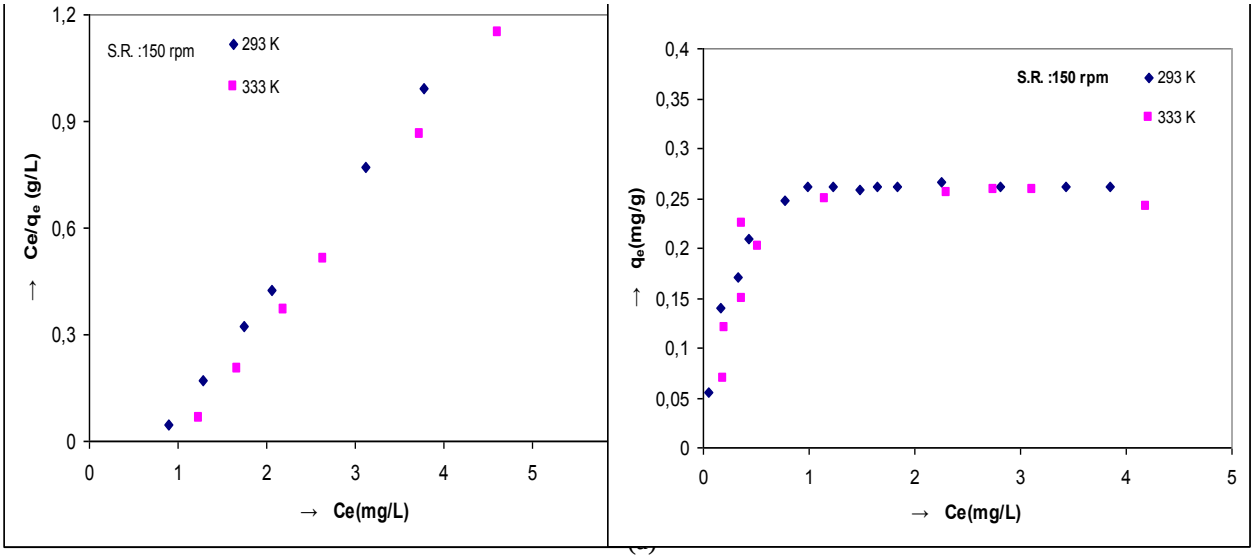

(b)

Figure 7. The Langmuir isotherm (a) and the Langmuir linear isotherm (b) of adsorption of chitosan and IC.

Experimental data which are related with the adsorption of chitosan and IC were applied to the following Langmuir linear isotherm equation:

$$C_a = {}_m\frac{bC_e}{1+bC_e}, \quad \frac{C_e}{C_a} = \frac{1}{C_m.b} \quad \overline{C_m} \qquad (8)$$

and the Langmuir constants (C_m and b) were calculated.

293 K		333 K	
C_m(mgg$^-$)	b(L.mg$^-$)	C_m(mgg$^-$)	b(L.mg$^-$)
0,3295	3,9620	0,3215	2,9942

Table 1. The Langmuir constants of the adsorption of chitosan and IC.

293 K			333 K		
ΔH (J.mol^{-1})	ΔG (J.mol^{-1})	ΔS (J.mol^{-1}K^{-1})	ΔH (J.mol^{-1})	ΔG (J.mol^{-1})	ΔS (J.mol^{-1}K^{-1})
-5680,8	-3353,8	-7,9421	-5680,8	-3036,2	-7,9417

Table 2. Thermodynamic parameters of the adsorption of chitosan and IC.

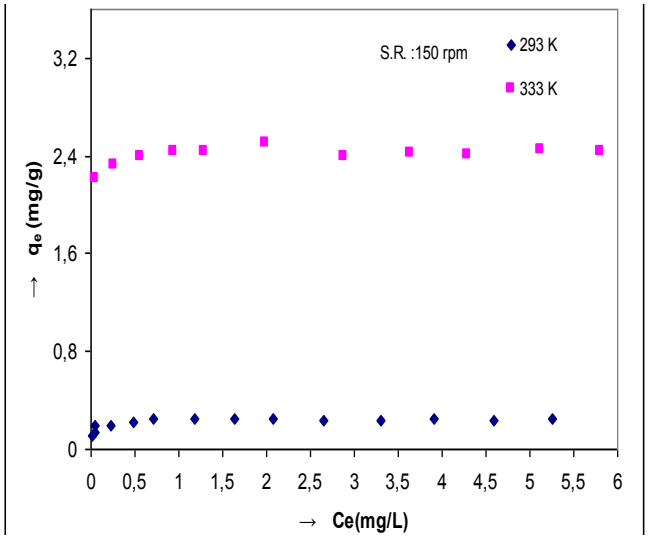

Figure 8. The isotherm of the adsorption of chitosan phthalate and IC.

According to **Figure 8**, the initial points of isotherms at both temperatures are on the ordinate. This situation is the indicator of strong chemical adsorption between IC and chitosan phthalate. As it is known, this kind of isotherm is called H-type isotherm according to isotherm classification made by Giles[15].

4. Conclusions

Chitosan adsorbed more IC at low temperature but chitosan phthalate adsorbed more IC at high temperature because of chemical adsorption. Chitosan phthalate removes IC more than chitosan. So, modifying chitosan with phthalate is advantageous.

References

1. Nandi BK, Gosvami A, Purkait MK. Adsorption characteristics of brilliant green dye on kaolin [J]. Journal of Hazardous Materials, 2009, 161, (1): 387-395.
2. Han X, Niu X, Ma X. Adsorption characteristics of methylene blue on poplar leaf in batch mode: Equilibrium, kinetics and thermodynamics [J]. Korean Journal of Chemical Engineering, 2012, 29, (4): 494-502.
3. Suchada Sawasdee, Hathairat Jankerd, Prachart Watcharabundit. Adsorption of dyestuff in household-scale dyeing onto rice husk [J]. Energy procedia, 2017, 138: 1159-1164.
4. Ensar Oguz, Bulent Keskinler, Ahmet Tortum. Determination of the apparent ozonation rate constants of 1:2 metal complex dyestuffs and modeling with a neural network [J]. Chemical Engineering Journal, 2008, 141, (1-3): 119-129.
5. Ahn DH, Chang W.S., Yoon T.I. Dyestuff wastewater treatment using chemical oxidation, physical adsorption and fixed bed biofilm process [J]. Process Biochemistry, 1999 (34): 429-439.
6. Yanfang Feng, Fan Yang and so on. Basic dye adsorption onto an agro-based waste material- sesame hull (sesamum indicum L.) [J]. Bioresource Technology, 2011, 102, (22): 10280-10285.
7. Lili Ren, Xiaoxia Yan and so on. Influence of chitosan concentration on mechanical and barrier properties of corn starch/chitosan films [J]. International Journal of Biological macromolecules, 2017 (15): 1636-1643.
8. Sudheesh K. Shukla, Ajay K. Mishra and so on. Chitosan-based nanomaterials: A state-of-the-art review [J]. International Journal of Biological macromolecules, 2013 (59): 46-58.
9. Wang Guanghui, Liu Jinsheng and so on. Adsorption of uranium (VI) from aqueous solution onto cross-linked chitosan [J]. Journal of Hazardous Materials, 2009 (168): 1053-1058.
10. Xu Jinsheng, Chen Mansheng and so on. Adsorption of uranium(VI) from aqueous solution by diethylenetriamine-functionalized magnetic chitosan [J]. Journal of Radioanalytical and Nuclear Chemistry, 2016 (307): 1135-1140.
11. Sten Yngve Lagergren, Zur Theorie der Sogenannten Adsorption Gel öster Stoffe, Kungliga Svenska Vetenskapsakademiens [M]. Handlingar (24): 1-39, 1898.
12. Joseph Mauk Smith, Chemical Engineering Kinetics [M] . Singapore McGraw-Hill press, 1987.
13. Walter J. Weber, J. Carrell Morris. Kinetics of adsorption on carbon from solution [J]. Journal of the Sanitary Engineering Division, 1963 (89): 31-60.
14. Ebru Birlik, Sibel Buyuktiryaki and so on. Selective Separation of Thorium Using Ion Imprinted Chitosan Phthalate Particles via Solid Phase Extraction [J]. Seperation Science and Technology, 2006 (41): 3109-3121.

15. Charles H. Giles, David Smith, Alan Huitson. A general treatment and classification of the solute adsorption isotherm. I. Theoretical [J]. Journal of Colloid and Interface Science, 1974 (47): 755-765.

Applied Chemical Engineering (2019) Volume 2 Issue 2
doi:10.24294/ace.v1i2.660

Dynamic Viscosity of Partially Carbonated Aqueous Monoethanolamine (MEA) from (20 to 150) ℃

Udara S. P. R. Arachchige, Bhupendra Singh, Kishan Prajapati, Morten C. Melaaen

Telemark University College, Porsgrunn, 3901, Norway.

ABSTRACT

Viscosities of liquid solutions of monoethanolamine (MEA), water (H_20), and carbon dioxide (CO_2) have been measured. The mass fraction of MEA was (10, 20, 30, 40, and 50)%, and CO_2 loading values was between (0.1 to 0.5) mol CO_2/mol MEA. The operating temperature was varied between (20 to 150) ℃. The available literature data for temperature range (25 to 80) ℃ for mass fraction of (20, 30 and 40)% were used to compare the measurement data. The dynamic viscosity increase with the increase of CO_2 loading and decrease with an increase of temperature. The measured data were compared with the data predicted from available regression equation for certain temperature range. Agreement between measured data and the correlation data was satisfactory.

Keywords: Monoethanolamine, Viscosity, CO_2 loading, Rheometer, Temperature effect

1. Introduction

The various types of amines such as Monoethanolamine (MEA), diethanolamine (DEA), N-Methyldiethanolomine (MDEA) have been used for gas treating systems in a wide variety of applications[1]. The information available in literatures related to the physical properties of amines is limited. The uses of physical properties are typically for calculating of column dimensions and mass transfer correlations in gas absorption process[2,3].

Moreover, dynamic viscosities of partially carbonated aqueous amines are rare to find in the literatures. However, some of the data are available with limited concentration values and limited temperature range. Weiland *et al.*[4] has performed the experiments for CO_2 loaded aqueous MEA for temperature for 25 ℃ with 10, 20, 30 and 40% mass concentration. However, they have performed the experiments only for temperature 25 ℃.

Scarcity of physical properties availability was motivated to perform the experiments. Solution viscosity is one of the main parameters when considering the gas absorption process. Most of the literatures are reported the data only to temperature 80 ℃ and for limited concentration values only. Amundsen *et al.*[5] has reported the viscosity data for temperature range from (25 to 80) ℃ for concentration of MEA 20, 30 and 40 % mass basis. However, they have considered the CO_2 loading values $\alpha \in$ [0.1, 0.5] for their experiments. Therefore, more viscosity values are missing in the range while considering the available data for aqueous MEA with CO_2 loaded. This reason motivated us to perform the experiments for this study.

Modeling and simulation of gas absorption process require number of parameter values that related to the mass transfer rate[4]. This work was taken to determine the dynamic viscosity of Monoethanolamine (MEA) which is mainly considered for gas absorption. The CO_2 loaded amine viscosities are analyzed for the solutions with the mass ration, $r \in$ [0.1, 0.5] and CO_2 loading, $\alpha \in$ [0.1, 0.5] at temperatures, $T \in$ [20, 150] ℃. The measured data were compared with the available literature data[5]. At the same time, data were compared with the correlation presented in Weiland *et al.*[4].

2. Experimental section

The pure MEA was purchased from Merck KGaA supplier. The purity of the amine is 99.5% (mass basis). Amine solutions are prepared to get total concentration of amine mixture as 10%, 20%, 30%, 40% and 50% mass basis. The mixture after adding amines and distilled water is well stirred to get uniformity of the solution.

Aqueous solutions of amines were prepared using degassed, purified water and amines. Sample concentration maintained by adding required portion of amine and water with the help of analytical balance that has an accuracy of $\pm 1 \cdot 10^{-7}$.The high CO_2 loaded samples, α = (>0.5), prepared by bubbling CO_2 gas through an unloaded solution at required mass flow rate of CO_2 for an appropriate period. The required CO_2 loaded samples were prepared by diluting

doi: 10.24294/ace.v1i2.660

of high CO_2 loading with an unloaded solution in an appropriate ratio to get required loading values, α = (0.1 to 0.5).

The high loaded amine solutions were analyzed using titration method to check the exact CO_2 loading value and the amine concentration. The 1 mol Ł$^{-1}$ HCl solution is used to perform the titration to check the mass concentration of the amine solution. The sample is prepared by adding 2 g of each prepared amine solution with de-ionized water until each sample became 100 cm^3 in total. The amount of amine present in the sample is calculated by using the amount of HCl used for the titration. The sample preparation for the loading analysis was carried out by mixing about (0.5 to 1.0) g of the loaded amine solution with 50 cm^3 each from 0.3 mol Ł$^{-1}$ $BaCl_2$ and 0.1 mol Ł$^{-1}$NaOH. Those samples were heated around 5 min to let CO_2 in the samples to react with $BaCl_2$ and make precipitate as $BaCO_3$, then cooled down in a water bath. Moreover, the precipitate is collected and added to the 100 cm^3 of de-ionized water and then titrated with 0.1 mol Ł$^{-1}$HCl solution until the mixture reached the equilibrium point. The mixture was heated to remove the all of the dissolved CO_2. Then, same mixture was used for back titration with 0.1 mol Ł$^{-1}$NaOH solution to check the amount of excess HCl. At last, the moles of HCl reacted with $BaCO_3$ precipitate was used to find the amount of CO_2 in the corresponding partially carbonated aqueous amine sample and subsequently the CO_2 loading value of the sample.

Dynamic viscosity was measured using MCR 101 Anton Paar double-gap rheometer. The viscometer was calibrated against the petroleum distillate and mineral oil calibration fluid which is purchased from Paragon Scientific Ltd. The calibration factor was decided according to the experimental value and given literature value. The low-temperature measurements (20 – 30) ℃ were achieved by applying cooling system Physica VT2 connected together with the rheometer setup. Without further purification, all these amines were used for experimental studies. The temperature range from (40 – 150) ℃ is measured without cooling system. Two different pressure values are used for the measuring process in order to avoid the water vaporization at high temperatures. First part of the process (20 – 80) ℃ was completed with pressure 1.01 bar and the second part of the process (90 – 150) ℃ is completed with a 4.5 bar pressure.

The measured data for the different amines are compared with those available from the literature. The results that are obtained from the experiments were compared with the regression viscosity values which are predicted by correlations for viscosity at different temperatures.

3. Results and discussion

The viscosity data for partially carbonated MEA solutions, mass ratio r ∈ [0.1, 0.5], are presented in the **Table 1**-**Table 5** respectively. Five different concentration levels considered with five different CO_2 loading values for complete temperature range.

Temperature (℃)	**CO_2 loading (mol CO_2/mol MEA)**				
	α = 0.1	α = 0.2	α = 0.3	α = 0.4	α = 0.5
20	1.46	1.49	1.51	1.54	1.58
25	1.31	1.34	1.37	1.43	1.48
30	1.16	1.19	1.21	1.22	1.25
40	0.93	0.96	0.98	0.99	1.04
50	0.74	0.77	0.79	0.83	0.87
60	0.65	0.67	0.69	0.72	0.75
70	0.56	0.59	0.63	0.66	0.69
80	0.47	0.49	0.52	0.55	0.58
90	0.41	0.43	0.46	0.53	0.55
100	0.37	0.38	0.42	0.46	0.48
110	0.34	0.36	0.39	0.42	0.44
120	0.31	0.33	0.36	0.39	0.4
130	0.27	0.29	0.32	0.34	0.36
140	0.25	0.26	0.28	0.3	0.31

150	0.22	0.23	0.25	0.28	0.29

Table 1. Viscosity of MEA with different CO_2 loading, r = 0.1

Temperature (℃)	**CO_2 loading (mol CO_2/mol MEA)**				
	α = 0.1	α = 0.2	α = 0.3	α = 0.4	α = 0.5
20	2.09	2.15	2.34	2.46	2.68
25	1.81	1.86	1.94	2.16	2.27
30	1.58	1.62	1.68	1.88	1.98
40	1.27	1.34	1.42	1.48	1.63
50	1.02	1.08	1.17	1.21	1.28
60	0.85	0.89	0.99	1.02	1.08
70	0.72	0.75	0.82	0.85	0.90
80	0.61	0.65	0.70	0.72	0.75
90	0.52	0.6	0.68	0.7	0.72
100	0.47	0.57	0.64	0.66	0.69
110	0.41	0.51	0.56	0.61	0.64
120	0.37	0.48	0.5	0.54	0.58
130	0.33	0.44	0.48	0.52	0.54
140	0.3	0.37	0.42	0.46	0.48
150	0.27	0.33	0.37	0.39	0.42

Table 2. Viscosity of MEA with different CO_2 loading, r = 0.2

Temperature (℃)	**CO_2 loading (mol CO_2/mol MEA)**				
	α = 0.1	α = 0.2	α = 0.3	α = 0.4	α = 0.5
20	3.33	3.49	3.82	3.97	4.21
25	2.87	2.94	3.14	3.47	3.76
30	2.47	2.56	2.72	2.94	3.27
40	1.92	2.04	2.09	2.39	2.67
50	1.55	1.61	1.66	1.87	2.22
60	1.25	1.31	1.38	1.52	1.81
70	1.02	1.08	1.16	1.24	1.51

80	0.84	0.89	0.99	1.05	1.26
90	0.76	0.82	0.95	1.01	1.16
100	0.64	0.72	0.82	0.93	1.07
110	0.57	0.66	0.75	0.86	0.96
120	0.5	0.58	0.64	0.72	0.84
130	0.44	0.52	0.6	0.68	0.75
140	0.38	0.46	0.53	0.59	0.64
150	0.34	0.4	0.46	0.52	0.58

Table 3. Viscosity of MEA with different CO_2 loading, r = 0.3

Temperature (℃)	**CO_2 loading (mol CO_2/mol MEA)**				
	α = 0.1	α = 0.2	α = 0.3	α = 0.4	α = 0.5
20	5.01	5.56	6.70	7.49	7.89
25	4.25	4.82	5.39	6.16	6.98
30	3.56	4.10	4.61	5.22	5.84
40	2.74	3.02	3.28	3.63	4.05
50	2.13	2.37	2.65	2.97	3.22
60	1.64	1.82	2.15	2.52	2.72
70	1.30	1.52	1.77	2.05	2.37
80	1.07	1.24	1.39	1.71	1.94
90	1.01	1.16	1.24	1.66	1.84
100	0.93	1.05	1.11	1.42	1.65
110	0.84	0.96	0.99	1.21	1.43
120	0.73	0.84	0.86	0.96	1.1
130	0.67	0.74	0.79	0.85	0.98
140	0.56	0.61	0.68	0.76	0.84
150	0.45	0.53	0.58	0.6	0.66

Table 4. Viscosity of MEA with different CO_2 loading, r = 0.4

Temperature (℃)	CO_2 loading (mol CO_2/mol MEA)				
	α = 0.1	α = 0.2	α = 0.3	α = 0.4	α = 0.5
20	7.49	9.66	11.60	14.30	16.66
25	6.14	7.91	9.48	11.30	13.50
30	5.14	6.56	7.83	9.37	11.35
40	3.72	4.60	5.92	6.78	8.05
50	2.79	3.52	4.30	5.20	5.96
60	2.15	2.78	3.09	4.09	4.55
70	1.72	2.27	2.49	3.37	3.62
80	1.40	1.89	2.06	2.91	3.27
90	1.24	1.57	1.89	2.65	2.89
100	1.10	1.30	1.64	1.96	2.61
110	0.96	1.16	1.32	1.74	2.28
120	0.86	1.01	1.18	1.46	1.96
130	0.74	0.96	1.04	1.30	1.64
140	0.65	0.82	0.95	1.13	1.42
150	0.56	0.63	0.73	0.84	1.12

Table 5. Viscosity of MEA with different CO_2 loading, r = 0.5

The viscosity data measured for loaded mixtures at temperature from 25 to 80 ℃ are compared with data from Amundsen *et al*.[5] in **Figure 1** to **Figure 3** for three different amine concentration. The literature data only available for temperature up to 80 ℃ and concentration, r = (0.2, 0.3, 0.4).

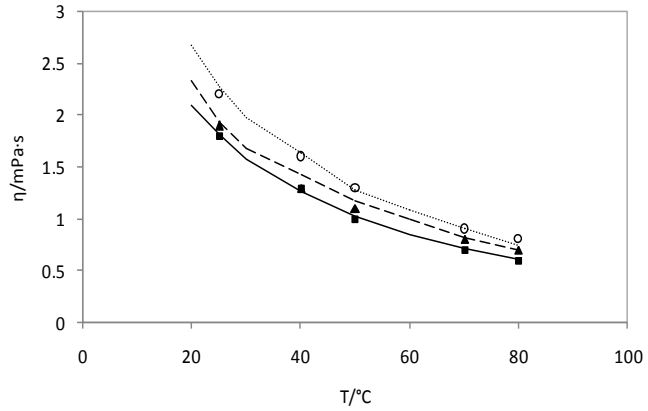

Figure 1. Viscosity variation with temperature, r = 0.2, Lines are experimental data: −, α = 0.1; - -, α = 0.3; ..., α = 0.5. Symbols refer to literature data: ■, α = 0.1; ▲, α = 0.3; ○, α = 0.5.

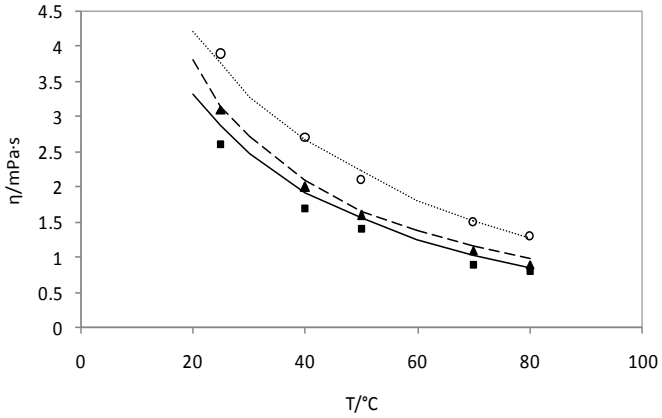

Figure 2. Viscosity variation with temperature, r = 0.3, Lines are experimental data: −, α = 0.1; - -, α = 0.3; ..., α = 0.5. Symbols refer to literature data: ■, α = 0.1; ▲, α = 0.3; ○, α = 0.5.

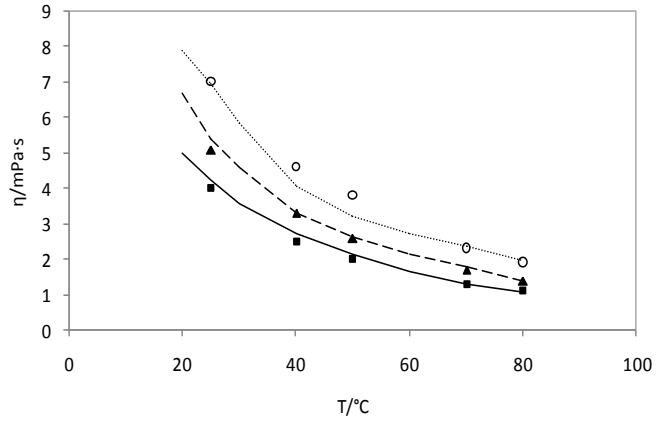

Figure 3. Viscosity variation with temperature, r = 0.4, Lines are experimental data: −, α = 0.1; - -, α = 0.3; ..., α = 0.5. Symbols refer to literature data: ■, α = 0.1; ▲, α = 0.3; ○, α = 0.5.

The literature data and experimental work in this study are in good agreement. The average absolute deviation (AAD) is 0.03 mPa s at r = 0.2, 0.04 mPa s at r = 0.3 and 0.003 mPa s at r = 0.4. The correlation suggested by Weiland *et al*. [4] is used to calculate the estimation values of viscosity for different temperatures (Equation 1).

$$\frac{\eta}{\eta_{H_2O}} = \exp\frac{\left[(aw+b)T+(cw+d)\right]\left[\alpha(ew+fT+g)+1\right]w}{T^2} \quad (1)$$

Where η and $\eta_{H2O}$are the viscosities of the amine mixture and water viscosity at that temperature respectively in mPa s. w is the mass percent of the solution, T is the operating temperature in K, and α is the CO_2 loading in amine mixture (mol CO_2/mol MEA). The required coefficients are given in the **Table 6**.

Parameter	Value for MEA
a	0
b	0
c	21.186
d	2373
e	0.01015
f	0.0093
g	-2.2589

Table 6. Parameters for solvent viscosity[4]

The equation can be used to calculate MEA solution viscosity up to amine concentration 40% mass basis with CO_2 loading up to 0.5 (mol CO_2/mol MEA) and to a maximum temperature 398 K[4]. Due to the limitations of applicability of the equation 1, experimental data are compared up to temperature 120 ℃ and r = (0.1, 0.2, 0.3, 0.4) solution concen-

tration. The required water viscosity for an above equation is taken from the previous studies[6]. **Figure 4, Figure 5**, **Figure 6** and **Figure 7** show the measurements from this work compared to the correlation viscosity values at T ∈ [20, 120] ℃ for amine solution mass ration, r ∈ [0.1, 0.4]. Figures show the viscosity (Y axis) variation with temperature (X axis) for different CO_2 loading values. The part of the experiential values is only compared with available regression viscosity values as it has limitations in equation.

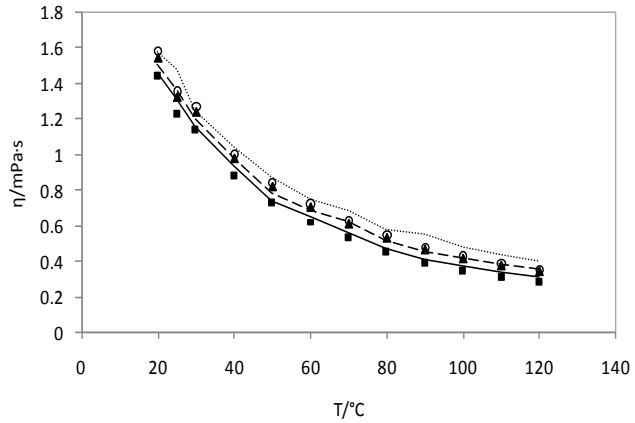

Figure 4. Viscosity variation with temperature, r = 0.1, Lines are experimental data: ─, α = 0.1; - -, α = 0.3; ..., α = 0.5. Symbols refer to regression data: ■, α = 0.1; ▲, α = 0.3; ○, α = 0.5.

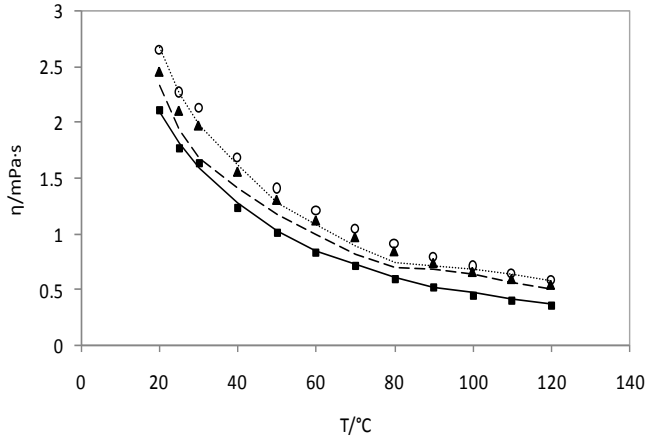

Figure 5. Viscosity variation with temperature, r = 0.2, Lines are experimental data: ─, α = 0.1; - -, α = 0.3; ..., α = 0.5. Symbols refer to regression data: ■, α = 0.1; ▲, α = 0.3; ○, α = 0.5.

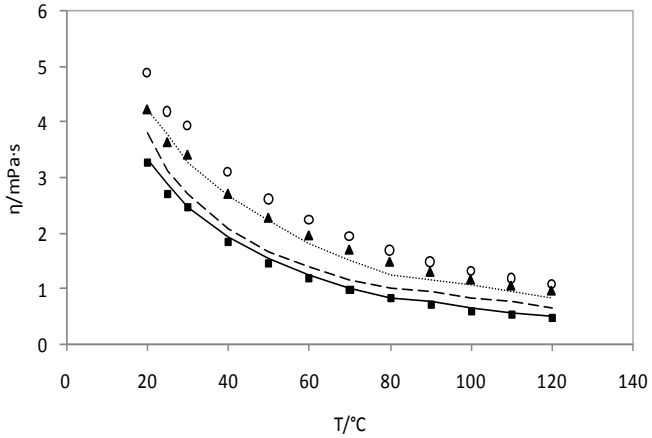

Figure 6. Viscosity variation with temperature, r = 0.3, Lines are experimental data: ─, α = 0.1; - -, α = 0.3; ..., α = 0.5. Symbols refer to regression data: ■, α = 0.1; ▲, α = 0.3; ○, α = 0.5.

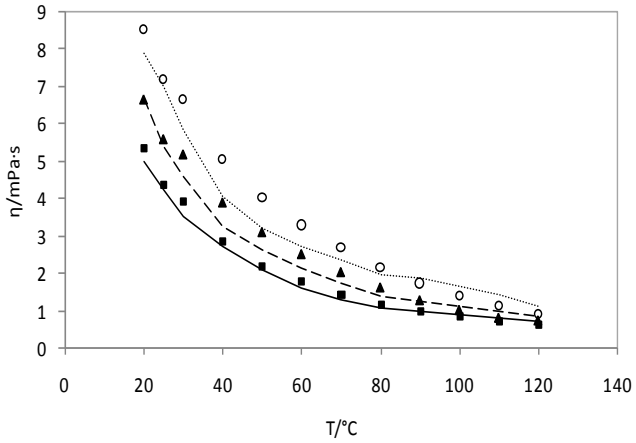

Figure 7. Viscosity variation with temperature, r = 0.4, Lines are experimental data: ─, α = 0.1; - -, α = 0.3; ..., α = 0.5. Symbols refer to regression data: ■, α = 0.1; ▲, α = 0.3; ○, α = 0.5.

The agreement between correlation results and this work in satisfactory. However, correlation shows over predicts for most of the viscosity values for every concentration. The average absolute deviation (AAD) between this work and equation regression data are 0.02, 0.09, 0.36, 0.19 mPa s respectively for mass fraction of amine, r = (0.1, 0.2, 0.3, 0.4).

4. Experimental uncertainties

The uncertainty of the viscosity measurements of CO_2 loaded aqueous amines arises as a combination of the uncertainty of the temperature measurements, sample preparation, CO_2 loading and measuring instrument uncertainties. The temperature accuracy, U(T), which is related to rheometer temperature controller, is given as ±0.3K. The maximum viscosity gradient against the temperature, $\Delta\eta/\Delta T$, is calculated as 0.040 mPa·s·K^{-1}. The corresponding uncertainty in η, $(\Delta\eta/\Delta T)\cdot\Delta T$, is then estimated as ±0.0120 mPa·s. The uncertainties of the sample preparation were found by calculating the error values (difference between the expected value and measured value r) of the prepared sample. The mass ratio uncertainty ±0.004, U(r), and the viscosity gradient ($\Delta\eta/\Delta r$) with 0.05 mPa·s are used for calculating the uncertainty of sample preparation. The resulting uncertainty in the sample preparation is calculated as, $(\Delta\eta/\Delta r).\Delta r$, ±0.00020. The uncertainty of loading, U(α), was found to be ±0.005 (mol CO_2/mol MEA) for MEA. The viscosity gradient, $\Delta\eta/\Delta\alpha$ was found as 2.1 mPa s (mol CO_2/ mol MEA)$^{-1}$. The corresponding uncertainty was calculated as $(\Delta\eta/\Delta\alpha)\cdot\Delta\alpha$, ±0.0105 mPa s. The rheometer accuracy is given as ± 0.002 mPa s. The overall uncertainty of η, U(η), is calculated by combining the partial uncertainties reported in this section with root sum of square method. The value is calculated as ±0.0161 mPa·s. The combined expanded uncertainty of the viscosity, Uc(η), is calculated as ±0.032 mPa s (level of confidence 0.95). The combined expanded uncertainty, suggested by symbol Uc, is obtained by multiplying overall uncertainty, U(η), by a coverage factor, suggested symbol k. Typically, k is assumed to be 2 with the level of confidence 0.95.

5. Conclusions

The dynamic viscosity of partially carbonated MEA solution was measured for the temperature range (20 to 150) ℃ for mass fraction (10 to 50)% and CO_2 loading (0.1 to 0.5) mol CO_2/mol MEA. The agreement with the literature data for temperature range (25 to 80) ℃ is satisfactory for mass fraction (20 to 40)%. The comparison between Weiland's proposed model and measurement data are in good agreement. However, regression model is valid only for mass fraction of MEA up to 40% and temperature up to 125 ℃. Therefore, measurement data were compared only for valid operating conditions. The AAD between this work and equation regression data are 0.02, 0.09, 0.36, 0.19 mPa s respectively for mass fraction of amine, r = (0.1, 0.2, 0.3, 0.4). However, Weiland's regression model can be used for estimation of viscosity inside the limitations. Further measurements have to perform for other amines as well.

References

1. Kohl, A. L., Nielsen, R. B.Gas Purification, 5th edition; Gulf Publishing Company: Houston, 1997.
2. Wang, G. Q., Yuan, X. G., Yu, K. T. Review of mass transfer correlations for packed columns. Ind. Eng. Chem 2005, 44, 8715-8729.

3. Eckert, J.S. Selecting the proper distillation column packing. Chem. Eng. Prog 1970, 66 (3), 39-44.
4. Weiland, R.H., Dingman, J.C., Cronin, D.B., Browning, G.J. Density and viscosity of some partially carbonated aqueous alkanolamine solutions and their blends. J. Chem. Eng. Data1998, 43, 378-382.
5. Amundsen, T. G., Øi, L. E., Eimer, D. A. Density and Viscosity of Monoethanolamine + Water + Carbon Dioxide from (25 to 80) ℃.J. Chem. Eng. Data 2009, 54, 3096-3100.
6. Arachchige, U. S. P. R., Aryal, N., Eimer, D. A., Melaaen, M. C.Annual Transactions - The Nordic Rheology Society 2013, 21, 299-308.

Applied Chemical Engineering

Focus and Scope

Applied Chemical Engineering is an international Open Access journal that publishes original research discoveries related to all areas of applied chemical engineering. This journal covers bioenergy, environmental chemical engineering, resources, pollution, reaction kinetics, chemical process, nanotechnology, bioreactors, catalysis, material synthesis, and other applied researches.

The *ACE* publishes original articles, research papers, review articles, reports, editorials, communication, brief commentaries, perspective articles, method, etc.

EnPress Publisher, LLC

EnPress Publisher, LLC, is a scholastic conduit for an assembly of professionals in the domains of science, technology, medicine, engineering, education, social sciences, and many more, as a round table for their intellectual discourse and presentation, and as an instrument to galvanize research designs, policy implementation, and commercial interests, to facilitate the prevailing over their challenges and to encourage to the full advantage of their resources and true potential.

We are the intellectual and academic home for academics, educators, scholars, clinicians, corporate researchers, who all play important roles in a wide range of national and international research organizations, and whose interests, expertise, research approaches, and industry objectives from around the world coalesce together to advance significant contributions in their research and professional fields.

As an instrument of information purveyor, we seek to combine academic rigor and originality with the nuanced development of policy and practice. Via our journals, client database, online campaigns, and social media presence, we offer a platform for industry professionals to interconnect, as well as opening doors towards cost-effective solutions for them to succeed, and we confidently hope to inspire a new generation of multidisciplinary researchers, think-tank experts, policymakers and business entities to innovate and advance their knowledge across fields.

EnPress Publisher, LLC

Add: 14701 Myford Road, Suite B-1, Tustin, CA 92780, United States

Tel: +1 (949) 299 0192

Email: contact@enpress-publisher.com

Web: https://enpress-publisher.com